Journal of Water Process Engineering 54 (2023) 104040

Contents lists available at ScienceDirect

Journal of Water Process Engineering

journal homepage: www.elsevier.com/locate/jwpe

Fabrication and characterization of recyclable, magnetic $(CoFe_2O_4)_x$/Ag_2S-ZnO composites for visible-light-induced photocatalytic degradation of methylene blue dye

Emmanuel O. Ichipi [a,*], António B. Mapossa [a], Ana Cristina F.M. Costa [b], Evans M.N. Chirwa [a], Shepherd M. Tichapondwa [a]

[a] *Water Utilisation and Environmental Engineering Division, Department of Chemical Engineering, University of Pretoria, Pretoria 0002, South Africa*
[b] *Academic Unit of Materials Engineering, Synthesis of Ceramic Materials Laboratory, Federal University of Campina Grande, Paraíba, Brazil*

ARTICLE INFO

Keywords:
Advanced oxidation processes
Combustion synthesis
Magnetic nanocomposites
Photodegradation
Recyclable photocatalysts

ABSTRACT

Magnetic $(CoFe_2O_4)_x$/Ag_2S-ZnO composites (where x = 0.25, 0.5, 0.75 and 1 wt% $CoFe_2O_4$) were successfully synthesised and investigated in the removal of methylene blue (MB) from aqueous medium under visible-light irradiation. X-ray diffraction (XRD) analysis confirmed the crystallinity of the as-synthesised materials and established the average crystal size of these materials to be <8.5 nm. Vibrating sample magnetometer (VSM) analysis confirmed that all cobalt ferrite doped nanocomposites exhibited ferrimagnetic behavior with saturation magnetization values varying from 6.55 to 40.52 emu/g being recorded. Near complete degradation (99 %) was attained when 1 gL^{-1} of $(CoFe_2O_4)_{0.5}$/Ag_2S-ZnO composite was added to a 10 ppm solution of methylene blue (MB) at neutral pH for 4 h of visible light irradiation. The catalyst showed good stability, removing 93.1 % of MB dye after five reuse cycles. The composite catalyst reported in this study is therefore a promising material for large-scale water and wastewater treatment processes.

1. Introduction

Dye polluted wastewater that commonly emanates from textile industries, which are regarded as one of the largest global polluters, poses serious environmental and health hazards [1]. Approximately 100,000 different types of dyes are used commercially with 700,000 tons being produced annually [2]. It is estimated that 15–50 % of azo-dyes used in the textile industry find their way into water bodies since they do not bind completely during textile production [3]. Dye polluted wastewater increases the chroma levels in water bodies which in turn blocks sunlight from penetrating through water, thereby causing an auxotrophic deficiency in photosynthesis and dissolved oxygen levels of aquatic life [1]. Besides the obvious negative aesthetic effects that dyes have on aquatic systems, exposure to dyes such as methylene blue (MB) results in the destruction of soil microbial consortia and nutrients, which inhibits the growth and germination rate of plants [4]. When inhaled or ingested, dyes act as carcinogenic agents and can cause severe damage to the bladder and respiratory system of human beings [5]. Other acute toxic effects of dye exposure to humans include irritation of the eyes and skin, dermatitis, conjunctivitis, occupational asthma and many other allergic reactions [6]. It is therefore essential to find sustainable treatment strategies capable of efficiently removing these recalcitrant dye compounds from aqueous systems. Due to their high solubility in water, dyes are considered as one of the most difficult organic pollutants to remove from water [7].

Conventional biological wastewater treatment technologies have been shown to be ineffective in degrading MB dye owing to its complex phenolic structure, which stabilizes it from microbial degradation [8,9]. Photocatalysis has emerged as one of the potential technologies capable of degrading and mineralizing these pollutants. It is generally regarded as a green, low-cost and environmental friendly water treatment technology which has fast reaction rates [10]. The process involves the activation of a semiconductor material by light irradiation resulting in the generation of highly reactive free radicals, which react with the target pollutants through chemical redox reactions [11]. In recent years, several semiconductor photocatalysts, such as TiO_2, ZnO, BiOCl, ZnS, CdS, g-C_3N_4 have been studied extensively and their efficacy towards numerous target pollutants has been determined [12,13]. However,

---

* Corresponding author.
E-mail address: u17227870@tuks.co.za (E.O. Ichipi).

https://doi.org/10.1016/j.jwpe.2023.104040
Received 27 March 2023; Received in revised form 4 June 2023; Accepted 9 July 2023

most of these semiconductors are limited to UV light activation due to their wide bandgaps (>3.0 eV) and relatively lower performance under visible-light activation [14]. The combination of diverse semiconductor materials with narrow bandgap transition metals and non-metals, including C, Mg, Ag, CdSe, Ge, Ni, CuS, PbS, GaAs, and Fe_2O_3, enables visible light activation in photocatalysis through the formation of heterojunction schemes like Z-scheme, S-scheme, p-n and others [15]. For instance, in the Z-scheme mechanism, one semiconductor absorbs photons, creating electron-hole pairs, while the other semiconductor acts as a mediator for charge transfer [16]. This arrangement facilitates the efficient separation and utilisation of excited charge carriers, leading to enhanced overall efficiency of the system [17]. Lavand and Malghe [18] reported that C-doped ZnO heterojunction exhibited improved performance in the degradation of malachite green under visible light irradiation. Nitrogen and Ag were single doped and co-doped on TiO_2 via an in-situ solvothermal method and investigated the degradation of aqueous MB and gas phase NH_3 under visible-light irradiation [19]. While N enhanced the surface area and morphology, the Ag constituent narrowed the overall bandgap and extended visible-light absorption. The improved visible light activated photocatalytic activity was ascribed to an overall narrowing of the bandgap, high generation of electron/hole (e^-/h^+) pairs, and slower recombination rate of the separated charges [11].

Serious concerns around the recovery and reuse of photocatalyst materials exist. These engineered materials are often developed at significant cost depending on the synthesis method used. Therefore, the ability to efficiently recover and reuse the material would make the process more economically viable. Additionally, if left untreated, the photocatalysts can contribute to the generation of post-treatment sludge. Previous reports have shown the difficulty in separating nanomaterials like TiO_2 and ZnO from aqueous medium through simple centrifugation and decantation methods due to their nanometric particle sizes that makes them partially soluble in water [20]. Alternative approaches for facile recovery and reusability of photocatalysts involve utilizing metal plates and glass substrates as supporting materials, onto which the photocatalytic materials are coated [21,22]. In the context of retrieving and separating photocatalysts from these support media, two common methods are employed: scraping and dissolution with subsequent precipitation. The obtained recovered photocatalyst can then undergo further processing or purification to enable its reuse [23]. It is important to note that the specific technique for recovery and separation can vary depending on factors such as the type of photocatalyst, substrate material, and intended application, as certain materials may necessitate additional steps for recovery and treatment. However, it has been demonstrated that incorporating magnetic properties through the development of composite photocatalyst materials facilitates easier recovery through the application of a magnetic force [24,25]. Fe_3O_4 and γ-Fe_2O_3 have been used as catalysts; however, they have limitations such as susceptibility to acidic and oxidative environments, insufficient thermal stability, increased charge recombination rate, and high electron resistance [26]. For example, Wu et al. [27] used a recyclable magnetic ternary ZnO/Fe_3O_4/g-C_3N_4 photocatalyst to degrade several monoazo dyes under visible light irradiation and obtained degradation efficiencies higher than 80 % after 5 recycle runs, with the material maintaining its magnetic properties. Another study exploring the photocatalytic activity of the $TmVO_4$/Fe_2O_3 nanocomposite for the degradation of AR14 and EBT, it was observed that the degradation efficiency decreased from 68.3 % to approximately 57.9 % after five recycling runs. This decline in efficiency can be attributed to the loss of active sites during the recovery process [28]. In contrast, $CoFe_2O_4$ nanoparticles exhibit exceptional chemical stability and have been widely applied across diverse disciplines. $CoFe_2O_4$ stands out due to its robust magnetic anisotropy, moderate magnetization, and high coercivity, even under moderate temperature conditions [29].

In this study, spinel structured cobalt ferrite ($CoFe_2O_4$) was chosen as the magnetic property imparting material due to its chemical stability and inherent photocatalytic properties as evidenced by its low bandgap energy which reportedly improve visible light activation [24,25,30,31]. A review paper by Mapossa et al. highlighted the high degradation efficiency and good saturation magnetism observed when $CoFe_2O_4$ was coupled to TiO_2 and ZnO under UV light irradiation [24]. Another study by Ichipi et al. showed the enhanced visible light activity of ZnO when it was coupled with Ag_2S, which imparted surface plasmon response (SPR) properties [32]. This Ag_2S-ZnO composite catalyst remained stable after several recycle runs; however, it was difficult to recover. The present study therefore focused on incorporating $CoFe_2O_4$ into Ag_2S-ZnO to form a magnetic ternary $(CoFe_2O_4)_x$/Ag_2S-ZnO (CF/A-Z) composite catalyst activated by visible light irradiation. The study utilized catalyst synthesis methods that had low energy consumption requirements, which promote development of sustainable technologies.

The binary Ag_2S-ZnO composite photocatalyst was prepared through a simple "green synthesis" hydrothermal method. While the $CoFe_2O_4$ was synthesised using the combustion method. These materials were then mixed with an ethylene glycol binder to form ternary CF/A-Z catalysts with varying ratios of CF. MB dye was used to simulate dye-contaminated wastewater and the photocatalytic degradation efficiency of the CF/A-Z was fully investigated under varying synthesis and experimental parameters.

2. Materials and methods

2.1. Materials

MB stock solutions were prepared using deionized water from a micromeg ELGA deionizer, purchased from Labotec, South Africa. Chemical precursors for silver sulphide ($AgNO_3$ ≥99.99 %, CAS-7761-88-8; Na_2S CAS-1313-82-2) and zinc oxide ($Zn(CH_3COO)_2{\cdot}2H_2O$ ≥99.99 %, CAS-5970-45-6) synthesis were obtained from Glassworld and chemical supplies Cc Company, South Africa. Cobalt nitrate hexahydrate (≥99.99 %, CAS-10026-22-9), iron nitrate nonahydrate (≥99.99 %, CAS-7782-61-8), urea (≥99.0 %, CAS-57-13-6), sodium hydroxide (≥98 %, CAS-1310-73-2), ethylene glycol (≥99.8 %, CAS-107-21-1) and methylene blue (CAS-122965-43-9) were all purchased from Sigma-Aldrich (Merck), South Africa. All chemicals and reagents were utilized without further purification.

2.2. Synthesis of photocatalyst materials

Ag_2S-ZnO (A-Z) nanocomposite powder was prepared according to the method previously described in literature [33]. In brief, A-Z was prepared hydrothermally using $Zn(CH_3COO)_2{\cdot}2H_2O$, $AgNO_3$ and Na_2S as precursors and solvents reagents, including sodium hydroxide, methanol and deionized water. This method involved a series of facile chemical steps including calcination, ultra-sonication, drying and grinding. Cobalt ferrite was synthesised using a simple combustion method. This synthesis technique makes use of thermodynamic concepts typically applied in the chemistry of propellants and explosives materials. In this study, stoichiometric mixtures containing compounds with the metal ions of interest which also serves as the oxidizing reagent were homogenised with a fuel, urea ($CO(NH_2)_2$), a reducing agent [34,35]. The stoichiometric amounts were calculated using the scheme below:

$$\begin{aligned}Co(NO_3)_2 \bullet 6H_2O + 2\left[Fe(NO_3)_3 \bullet 9H_2O\right] + x\left[CO(NH_2)_2\right] \\ \rightarrow CoFe_2O_4 + (2x)[H_2O] + (24+2x)[CO_2] + (4+x)N_2\end{aligned}$$

The precursors were placed in a ceramic crucible, which was charged in a furnace set at 750 °C. Within 3 min of exposure, a highly exothermic and explosive reaction occurred. The resultant product was ground into a powder and passed through a 35 μm sieve.

2.3. Synthesis of $(CoFe_2O_4)_x/Ag_2S$-ZnO nanocomposites

$(CoFe_2O_4)_x/Ag_2S$-ZnOcomposites (where x = 0.25, 0.5, 0.75 and 1 wt% of CF) were prepared by mixing the required quantities of each synthesised constituent compound into 100 mL ethylene glycol (EG). The mixture was stirred for 30 min followed by ultra-sonication at 60 °C for 2 h after which the slurry was dehydrated overnight in an oven. The dried agglomerates were ground to a powder and further dried in an oven at 80 °C for 8 h to degrade the EG component completely. A scheme of the preparation of $(CoFe_2O_4)_x/Ag_2S$-ZnO nanocomposites is illustrated in Fig. 1a.

2.4. Material characterization

A PANalytical X'Pert Pro powder X-ray diffractometer with Co-K_α radiation ($\lambda = 1.789$ Å) in θ–θ configuration, measuring from 20° to 90° was used to identify the various phases present in the composite photocatalyst and its constituents. X'pert Highscore plus software database was used to match the obtained patterns to the database. A Zeiss Ultra PLUS FEG scanning electron microscope (SEM) was used to investigate the morphological properties of the nanocomposites. Images of the microstructures of the nanocomposites were further analysed using a JOEL JEM 2100F, 200 kV transmission electron microscope (TEM). The specific surface area and pore sizes of the nanocomposites were analysed using a TriStar II 3020 Version 3.02 Brunauer-Emmett-Teller instrument. A Hitachi U-3900 double beam single-monochromatic system installed with a UV-solutions software program was used to collect the ultraviolet-visible diffuse reflectance spectra (UV–vis DRS) of the synthesised materials. The absorption peaks were captured in the wavelength range 300 to 800 nm. The photoluminescence spectra and emission potential of the nanocomposite materials was determined using a FlouroMax-4 spectrofluorometer series, HORIBA scientific and detected with a photomultiplier R928P within spectral coverage ranging from 420 to 460 nm. Raman spectra were recorded using aWITec alpha 300 RAS+ Confocal micro-Raman microscope (Focus Innovations, Germany) with the laser wavelength set at 532 nm over a 180 s spectral acquisition time and laser power of 5 mW. A MicroSense 7404 model vibrating sample magnetometer (VSM) with a maximum applied magnetic field of 13,700 G was used to obtain the hysteresis loops of all the samples at room temperature (~23 °C).

2.5. Reactor setup and photocatalytic tests

The reactor setup was previously described in detail [32]. In summary, the experimental setup involved a wooden box containing three Philips 18 W fluorescent daylight lamps, each emitting a luminous flux of 1200 lm. The interior of the box was lined with aluminum foil paper to ensure uniform distribution and reflection of light. Two Teflon lined overhead stirrers were positioned approximately 15 cm away from the lamps to agitate two separate batches of the slurry solution continuously. The light intensity was determined by calculating the wattage of the lamps and the distance between the reactor and the lamp, resulting in a value of 142.857 W/m^2. The temperature of the reaction was monitored by placing a thermometer inside the box, indicating a temperature of 30 °C (±5). Based on the power ratings of the simulation lamps, the total energy consumption for a photocatalytic system per hour was estimated as 0.072 kWh. The temperature of the reaction was monitored using a thermometer placed inside the box, which indicated a temperature of 30 °C (±5). The photocatalytic activity of the synthesised $(CoFe_2O_4)_x/Ag_2S$-ZnO nanocomposites was studied by degrading methylene blue dye solutions under simulated visible light irradiation. For each batch test, 1 gL^{-1} of the photocatalyst was added to 200 mL of 10 ppm MB dye solution and stirred in the dark for 30 min to reach adsorption-desorption equilibrium. After which, the visible-light lamps were turned on under continuous stirring for a further 4 h for photocatalytic degradation to occur. To monitor the progressive degradation of MB dye, 2 mL samples were withdrawn from the reactor at 30 min intervals, centrifuged and measured using a BioChrom WPA lightwave II UV–Visible Spectrophotometer (λ_{max} = 663 nm). The percentage dye removal after the retention time was estimated by the following

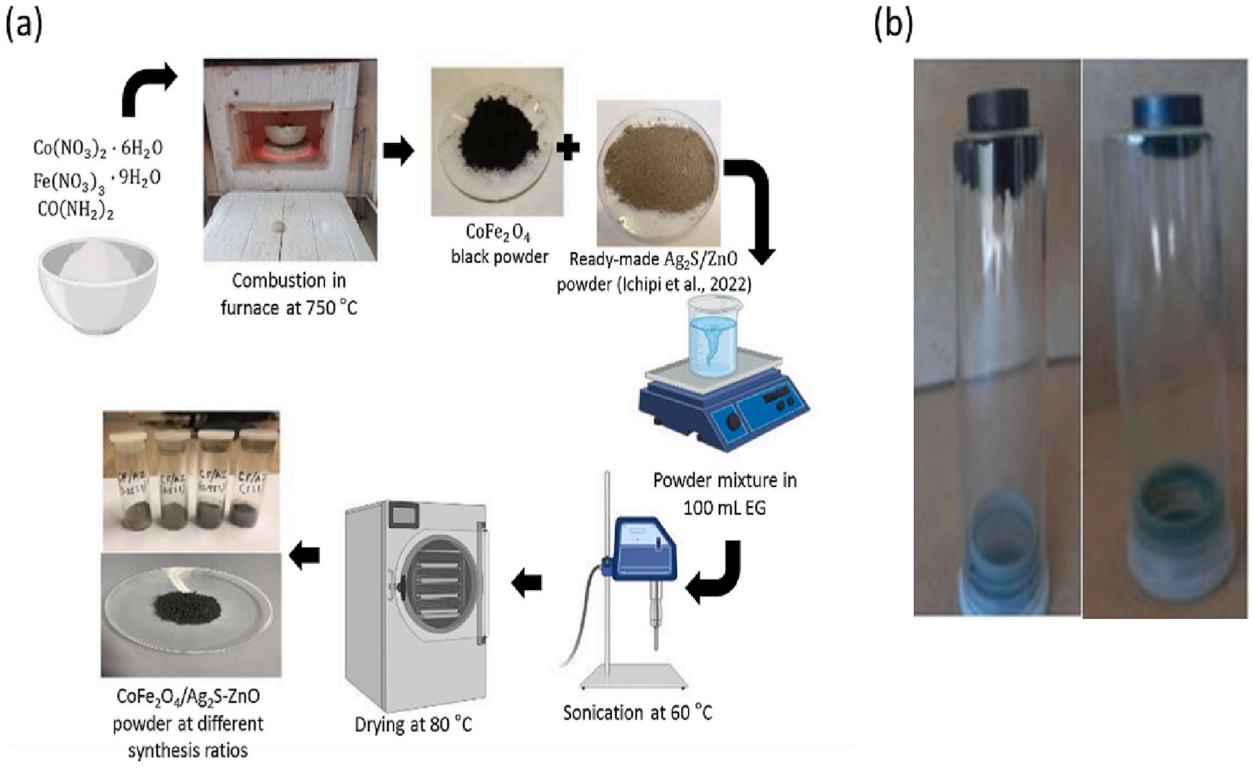

Fig. 1. (a) Pictorial illustration of the synthesis of $(CoFe_2O_4)_x/Ag_2S$-ZnO nanocomposites, (b) demonstration of photocatalyst magnetism.

expression represented by Eq. (1):

$$\%Degradation = \left(1 - \frac{C_t}{C_0}\right) \times 100 \tag{1}$$

where C_0 is the initial MB dye concentration before and C_t the final MB dye concentration after irradiation time, t.

Five recycle runs were conducted in order to determine the reusability and stability of the optimum $(CoFe_2O_4)_x/Ag_2S$-ZnO photocatalyst. After each run, the stirrers were stopped for 30 min to allow the catalyst particles settle by sedimentation after which, a handheld magnet was used to recover the material for the subsequent run as demonstrated in Fig. 1b. Free radicals and photo-generated charges diagnostic trapping tests were conducted to further investigate the photodegradation mechanism. Scavengers of the photo-induced reactive species ($OH^•$, O_2^-, h^+, and e^-) were added to the MB dye solution before the degradation experiments in order to determine the rate-limiting step. The scavenging tests were conducted by adding a concentration of 5×10^{-3} mol/dm^3 of isopropyl alcohol (IPA for the $OH^•$ radicals), p-benzoquinone (pBZQ for the O_2^- radicals), triethanolamine (TEA, for h^+_{VB}) and Cupper (II) nitrate (C_2N for e^-_{CB}).

3. Results and discussion

3.1. Crystalline phase identification

The X-Ray diffractometer patterns presented in Fig. 2 show the crystalline and structural phase of the synthesised $(CoFe_2O_4)_x/Ag_2S$-ZnO nanocomposites and its constituent materials. The expected major diffraction peaks for ZnO were observed at planes (100), (002), (101), (102), (110) and (103), which are characteristic of pure hexagonal wurtzite ZnO crystal according to JCPSD, card #36-1451. The small peak on plane (121) was attributed to the presence of Ag_2S. The low concentration and crystallinity of the Ag_2S compared to the other constituents of the nanocomposite could account for the limited detection of this characteristic peak. Additionally, the small particle size of silver sulphide (typically range between 2 and 5 nm) is significantly lower than the minimum XRD beam penetration depth (2–3 μm) depth. The x-ray beam therefore penetrates through the Ag_2S nanoparticles deposited on the surface and renders them undetectable [36]. $CoFe_2O_4$ characteristic peaks were detected on planes (220), (331) and (511), which corresponds to JCPSD card #21-0569. The diffraction patterns observed in the various $(CoFe_2O_4)_x/Ag_2S$-ZnO nanocomposites reveal the presence of three distinct phases: the cubic spinel phase of cobalt ferrite, the wurtzite hexagonal phase of zinc oxide, and the cubic (FCC) phase of silver sulphide [37]. Notably, a linear decrease in the lattice parameter of the cubic spinel phase was observed as the $(CF)_x$ content of the nanocomposites was increased. At lower $(CF)_x$ content, the substitution of Co_2^+ and Fe_3^+ ions by Zn_2^+ ions occurs within the lattice, leading to the formation of a non-stoichiometric cubic ferrite phase. This ion exchange process causes the crystal lattice to undergo expansion, resulting in an increase in the lattice parameter. These changes in lattice parameter can be attributed to the interexchange of metallic ions between the spinel and wurtzite phases. [38]. The crystallite size of the various nanocomposites was estimated using the most intense peaks using the Scherrer's formula expressed as Eq. (2):

$$D = \frac{K\lambda}{\beta cos\theta} \tag{2}$$

where D is the crystallite size of the nanoparticle, K is the Scherrer constant (approx. 0.94 for spherical crystals with cubic symmetry), λ is the X-ray wavelength (Co-K_α radiation = 1.789 Å), β is the line broadening full width at half maximum (FWHM) in radians and θ is the Bragg's angle in degrees half of 2θ. The crystallite sizes of the constituents, $CoFe_2O_4$ and Ag_2S-ZnO were determined based on most intense peaks at 2θ angles 41.4° and 42.7° which correspond to the (331) and (101) planes were calculated to be 1.17 nm and 8.23 nm, respectively. The crystallite sizes of the composite catalyst decreased from 4.26 to 3.97 nm as the amount of $CoFe_2O_4$ increased in the composite (Table 1).

Table 1

Summary of the BET surface area, estimated particle and crystallite size and calculated bandgap energies for the various nanocomposite photocatalysts and their constituent compounds.

Catalyst composites	S_{BET} (m^2g^{-1})	D_{BET} (nm)	Pore volume (cm^3g^{-1})	Crystallite size (nm)	Bandgap estimate (eV)
ZnO	7.78	137.46	0.026	8.52	2.2
$CoFe_2O_4$	34.05	33.25	0.184	1.17	3.26
$(CoFe_2O_4)_{0.5}$/ZnO	27.36	41.37	1.402	4.98	2.45
Ag_2S-ZnO	18.9	56.59	0.049	8.23	3.34
$(CoFe_2O_4)_{0.25}/Ag_2S$-ZnO	38.5	29.41	1.263	4.26	3.12
$(CoFe_2O_4)_{0.5}/Ag_2S$-ZnO	35.04	32.31	1.251	4.11	3.2
$(CoFe_2O_4)_{0.75}/Ag_2S$-ZnO	33.53	33.76	1.338	4.02	3.29
$CoFe_2O_4/Ag_2S$-ZnO	32.8	34.52	1.347	3.95	3.32

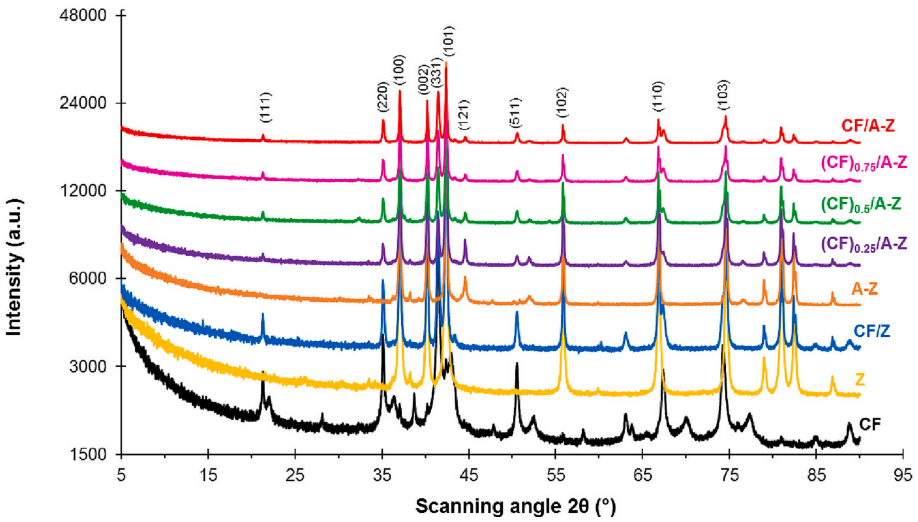

Fig. 2. XRD patterns for $CoFe_2O_4$, ZnO, Ag_2S-ZnO and $(CoFe_2O_4)_x/Ag_2S$-ZnO nanocomposites.

3.2. Morphology study

Scanning electron microscope (SEM) and transmission electron microscope (TEM) micrographs of the nanocomposites were captured to investigate the morphology of the materials. Fig. 3(a) shows that the $CoFe_2O_4$ was composed of porous flake-like agglomerates with pores with an average diameter of ~8 nm. The SEM image for Ag_2S-ZnO in Fig. 3(b) showed a mixed agglomerate of angular/cube like particles with an average size of about 25 nm. The various $(CoFe_2O_4)_x/Ag_2S$-ZnO nanocomposites in Fig. 3(c–f), showed clusters of both $CoFe_2O_4$ and Ag_2S-ZnO. The constituents retained in their individual micrographic morphologies. However, it was observed that at a higher concentration ratio of $CoFe_2O_4$, there was more aggregation and less porosity between the nanoparticles. The data extracted from the energy-dispersive X-ray (EDX) spectroscopy images and table in Supplementary information S1 and S2 showed a uniform distribution of each constituent chemical compound present in the various nanocomposites. The TEM images of all the synthesised nanocomposites are shown in Fig. 3(g–l). $CoFe_2O_4$ in Fig. 3(g) comprised of nanosized spherical particles clumped together into agglomerates while the Ag_2S-ZnO featured angular particles. TEM images presented in Fig. 3(i–l) showed good dispersion and interaction between the $CoFe_2O_4$ and Ag_2S-ZnO nanocomposite constituent materials. The darker parts of the images signify an electron-dense region of nanoparticles (<100 nm) that could not be transmitted by the electron beam.

3.3. Textural characterization via N_2 adsorption/desorption at 77 K

The BET specific surface area (S_{BET}) of the nanocomposites was measured and the equivalent particle size (D_{BET}) based on the theoretical density (ρ) of $CoFe_2O_4$ constituent was calculated following the expression [39] represented by Eq. (3):

$$D_{BET} = \frac{6000}{\rho S_{BET}} \tag{3}$$

Table 1 shows a continuous decrease of specific surface area of the nanocomposites from 38.5 to 32.8 m^2g^{-1} with an increase in cobalt ferrite (CF) constituent. This observation was somewhat surprising since pristine CF had a higher BET surface area (34.05 m^2g^{-1}) compared to Ag_2S-ZnO (18.09 m^2g^{-1}). Therefore, it would have been postulated that the BET surface area of the composite catalysts would increase with an increase CF composition. The decrease in BET surface area upon combining CF with AZ can be attributed to multiple factors. Firstly, the aggregation of CF nanoparticles occurs due to the influence of van der Waals forces and magnetic interactions among the particles. This aggregation leads to the formation of larger clusters, resulting in a reduced surface area compared to individual nanoparticles. Secondly, the presence of surface irregularities and roughness on CF nanoparticles contributes to the occurrence of vacancy defects, which diminish the porous structure and further decrease the surface area [40]. Lastly, the crystal structure of CF, which adopts a spinel-type configuration with metal cations occupying tetrahedral and octahedral sites in the lattice, limits the accessibility of the surface and impedes the development of a substantial surface area [40,41]. All cobalt ferrite containing composites

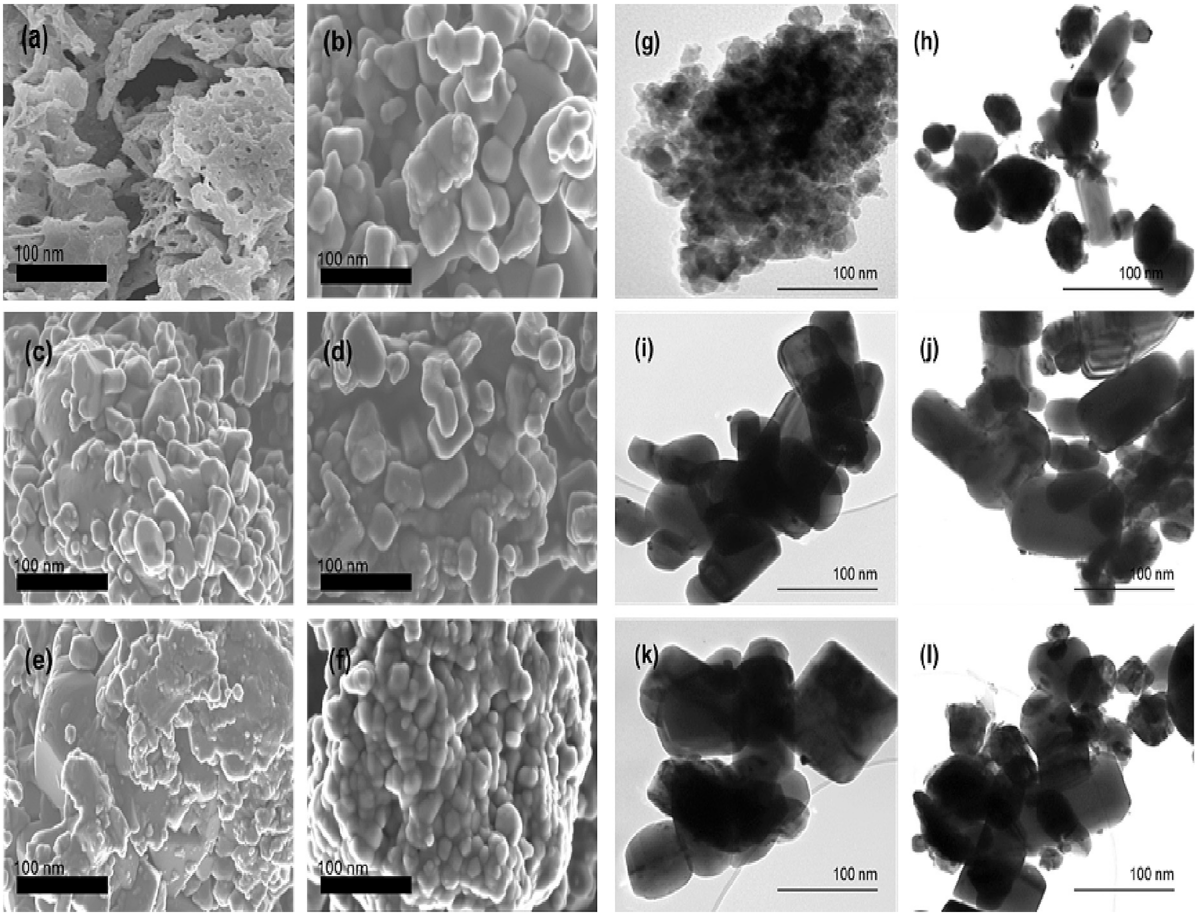

Fig. 3. SEM micrographs for (a) $CoFe_2O_4$; (b) Ag_2S-ZnO; (c) $(CoFe_2O_4)_{0.25}/Ag_2S$-ZnO; (d) $(CoFe_2O_4)_{0.5}/Ag_2S$-ZnO; (e) $(CoFe_2O_4)_{0.75}/Ag_2S$-ZnO; (f) $CoFe_2O_4/Ag_2S$-ZnO nanocomposites and High-resolution TEM micrographs for (g) $CoFe_2O_4$; (h) Ag_2S-ZnO; (i) $(CoFe_2O_4)_{0.25}/Ag_2S$-ZnO; (j) $(CoFe_2O_4)_{0.5}/Ag_2S$-ZnO; (k) $(CoFe_2O_4)_{0.75}/Ag_2S$-ZnO and (l) $CoFe_2O_4/Ag_2S$-ZnO nanocomposites.

present a similar pore size distribution regardless of the $CoFe_2O_4$ to ZnO ratio used. The calculated micropores for ZnO and Ag_2S-ZnO particles were 0.026 and 0.049 cm^3g^{-1}, respectively. Fig. 4 shows the N_2 adsorption-desorption isotherms hysteresis loops of all the as-synthesised magnetic $(CoFe_2O_4)_x/Ag_2S$-ZnO nanocomposites. The hysteresis loops of all the magnetic nanocomposites can be described as a Type IV BET isotherm, which is a common occurrence for mesoporous solids. Typically, multilayer adsorption occurs on the surface of the solids proceeded by capillary condensation in the mesopores with a limiting uptake over a range of relative pressure. Adsorption reaches a point of saturation quantity absorbed ($mmolg^{-1}$) and starts desorbing with relative pressure (p/p^0) to form the hysteresis loop. Monolayers followed by multilayers are typically formed at low-pressure regions.

3.4. Diffused reflectance spectrometry study

The optical properties of the synthesised photocatalysts were examined by UV–vis DRS and the results are shown in Fig. 5. A clear difference in the absorption spectra of $CoFe_2O_4$ compared to the other magnetic CF/A-Z nanocomposites was observed. The absorption peak of $CoFe_2O_4$ occurred at about 300 nm, which affirms that the material is photo-responsive in the UV light wavelength [42]. While, ZnO had absorption peak in the UV light range at about 380 nm, but it was noticed to have red-shifted towards the visible light region upon the addition of Ag_2S. The shifting of absorption peaks towards a higher wavelength can be attributed to the narrowing of bandgap levels due to the SPR photonic effect of the Ag compound. Tauc plots of absorbance were applied to estimate the bandgap energy of the nanocomposites following the expression represented by Eq. (4).

$$(\propto hv)^n = A\left(hv - E_g\right) \tag{4}$$

where '∝' is the absorption coefficient, 'n' represents the type of transition (direct for metallic semiconductors, n = ½), 'hv' is the photon energy (1240 nm^{-1}), 'A' is the constant and 'E_g' is the bandgap energy.

Tauc plots were used to estimate was established by extrapolating a linear intercept of graph $(\propto hv)^n$ vs hv as shown in the supplementary data provided (S3). The direct bandgap energy of all the as-synthesised nanocomposites are presented in Table 1. The photosensitivity of the nanocomposites continuously blue-shifted towards UV range with an increase of cobalt ferrite. Quantum size effect is significant for semiconductor nanoparticles, such that; the overall bandgap increases rapidly with a decreasing particle size. This results in an interband spacing transition (blue-shifting) of photosensitivity towards the UV region [43]. As the particle approaches the nanoscale size, the number of overlapping orbitals (energy level) decreases causing the band to be thinner. Consequently there is an increased proximity of the electron hole pairs (e^-/h^+) yielding a significant overall kinetic energy in their columbic interaction [44]. The widening of bandgap energy of the magnetic $(CoFe_2O_4)_x/Ag_2S$-ZnO nanocomposites can be attributed to a reduction of their quantum size relative to the combination ratio of $CoFe_2O_4$ as formerly confirmed by the XRD results presented in Table 1.

3.5. Photoluminescence study

The PL emission spectra of the as-prepared nanocomposites in Fig. 6 was conducted at an excitation wavelength of 320 nm under room temperature. Effective degradation using the photocatalytic nanocomposites is subject to absorption of light photons, which excites the movement of electrons leading to intrinsic oxygen defects and vacancies [45]. When $CoFe_2O_4$ was combined with ZnO at a 1:2 ratio, the band peak shifted slightly to 438 nm due to intra-bandgap oxygen defects. However, it is noticed that the band peak shifted to 441 nm for all the $(CoFe_2O_4)_x/Ag_2S$-ZnO nanocomposites which can be attributed to the presence of photonic Ag_2S in the ternary composite. The PL emission spectrum for $CoFe_2O_4$ (435 nm) had the highest intensity at 108000 while Ag_2S-ZnO (441 nm) had the lowest intensity of 62,000. This indicates that the Ag_2S-ZnO constituent had the lowest rate of electron-hole recombination while CF had the highest rate [46]. Theoretically, this suggests that of all the material under investigation in this study, CF should present the worst photocatalytic degradation efficiency with Ag_2S-ZnO showing the best. All the $(CoFe_2O_4)_x/Ag_2S$-ZnO composite catalysts should feature intermediate degradation properties since their PL intensities lies between those of the two primary constituent materials.

3.6. Raman light scattering spectroscopy

The Raman scattering spectra in Fig. 7 shows the existence of an

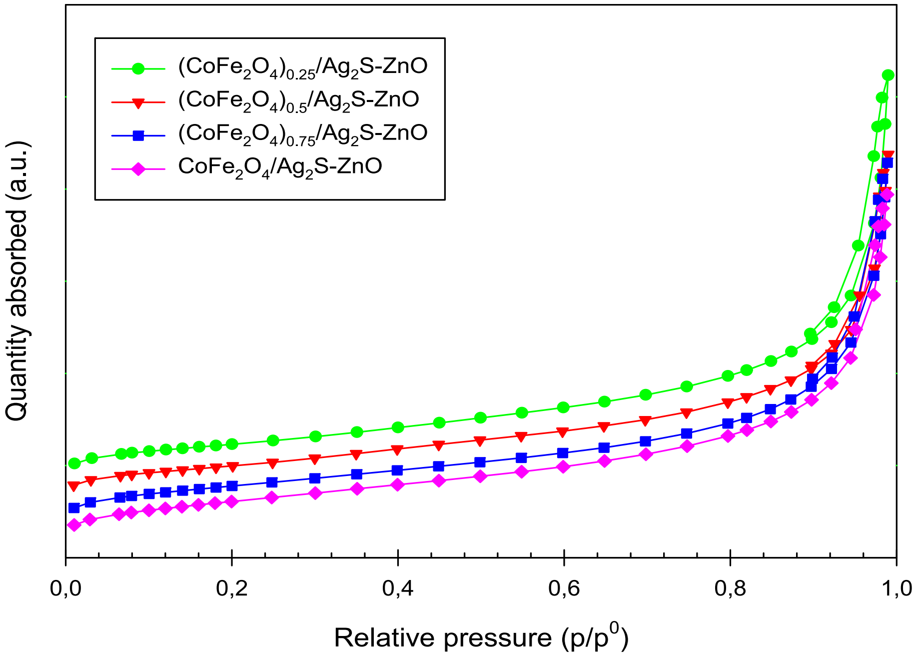

Fig. 4. N_2 adsorption-desorption isotherms for all the magnetic $(CoFe_2O_4)_x/Ag_2S$-ZnO nanocomposites.

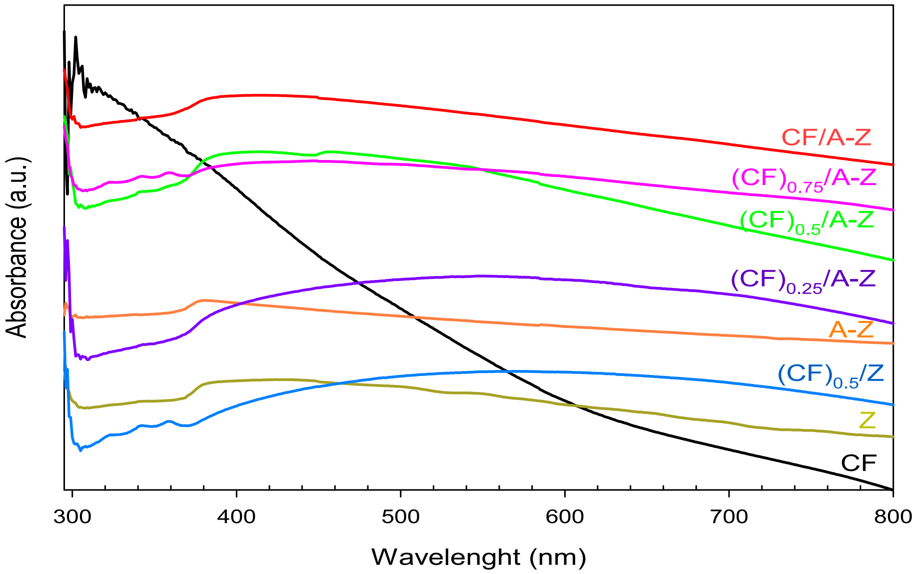

Fig. 5. UV–vis absorption spectra of all the synthesised nanocomposites.

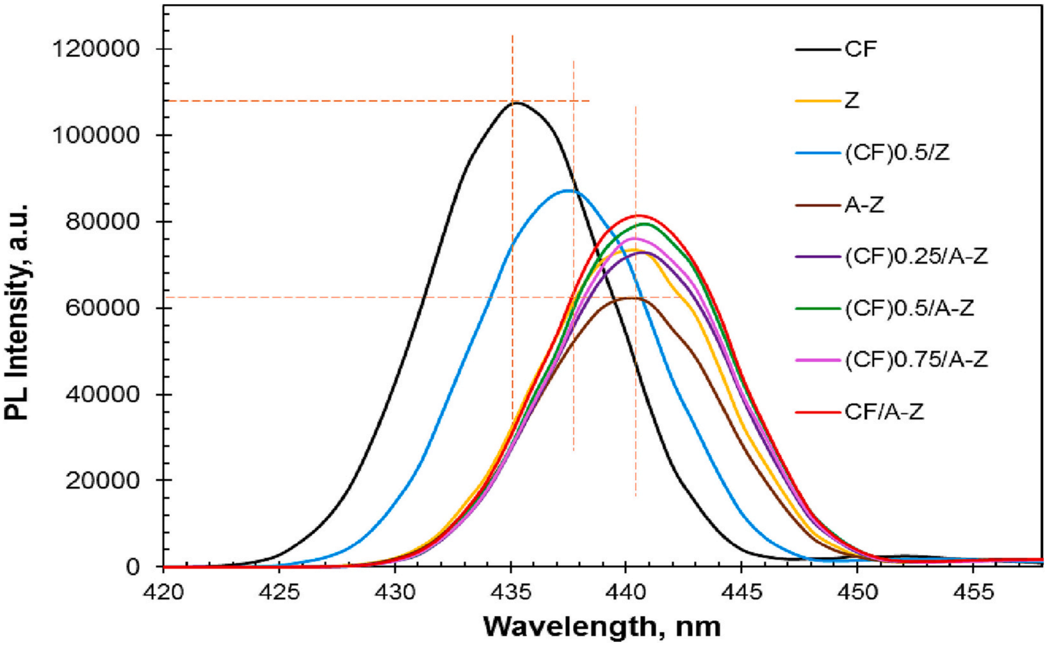

Fig. 6. Photoluminescence spectra for all the synthesised $(CoFe_2O_4)_x/Ag_2S$-ZnO nanocomposites.

inverse spinel configuration of $CoFe_2O_4$ excluding any peak that signifies the formation of any impurities during its synthesis. The band peaks at 655 cm^{-1} and 767 cm^{-1} correspond to the A_{1g} tetrahedral symmetrical stretching of the O_2 atoms relative to the Co and Fe ions present in the composite [47]. The bands at 493 cm^{-1} and 274 cm^{-1} are assigned to the T_{1g} asymmetrical stretching mode of the tetrahedron and E_g symmetrical bending of Fe(Co)-O ions. The major peaks of the ZnO spectra at about 485 cm^{-1} and 95 cm^{-1} are assigned to the 1st-order E_1 mode optical phonon and the 2nd-order E_2 mode low boundary phonons which affirms the wurtzite hexagonal phase of ZnO [48]. The formation of ZnO-O—Ag_2S bond suggests a strong interaction between their polarized charges features corresponding to a higher order light scattering intensity [49]. In the $(CoFe_2O_4)_x/Ag_2S$-ZnOnanocomposites a similar spectra pattern is observed with enhancement in intensity of the major peak at 65 cm^{-1} and 578 cm^{-1} relative to an increase in $CoFe_2O_4$ constituent. This is attributed to the incorporation of Co and Fe ions from the cubic spinel structure to the Ag_2S-ZnO structure since the hexagonal structure of ZnO is highly sensitive to lattice strain [38].

3.7. Magnetic properties

The magnetic hysteresis (M-H) loops of the synthesised photocatalyst samples are shown in Fig. 8. Different values of the magnetic parameters such as remanent magnetization (M_r), saturation magnetization (M_S), coercivity (H_C) were extracted as indicated inset Fig. 8, and the squareness ratio (SQ = M_r/M_s) was estimated. The expansion of the M-H loops along the magnetic field axis of CF was due to the exchange coupling of diamagnetic interfaces (FM-AFM) and/or random circulation of magnetic nanoparticles within the material known as exchange bias (H_{EB}) [50]. The experiential exchange bias in the nanocomposites were postulated to be due to an external anisotropy source from Ag_2S-ZnO, such that the orderly magnetic spins of $CoFe_2O_4$ kept moving

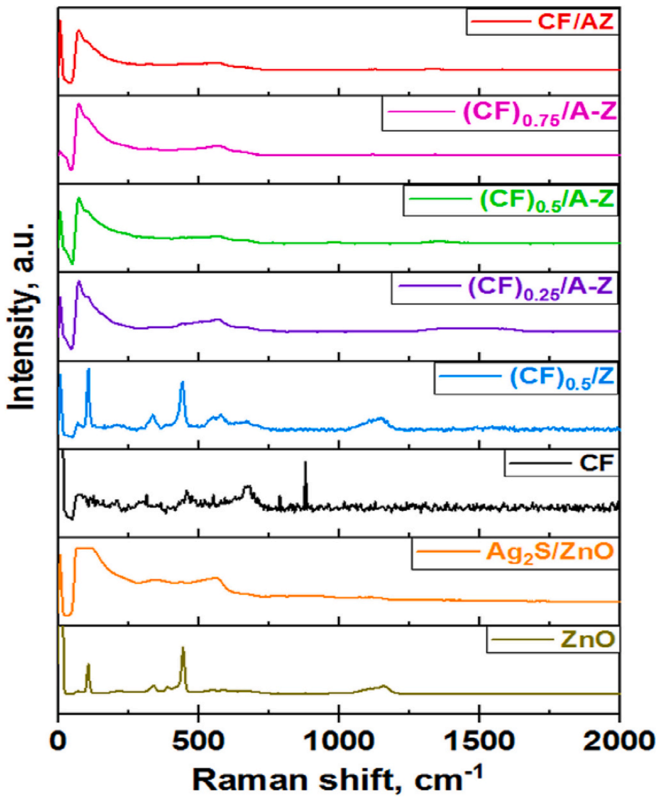

Fig. 7. Raman light-scattering spectra for all the synthesised $(CoFe_2O_4)_x/Ag_2S$-ZnO nanocomposites.

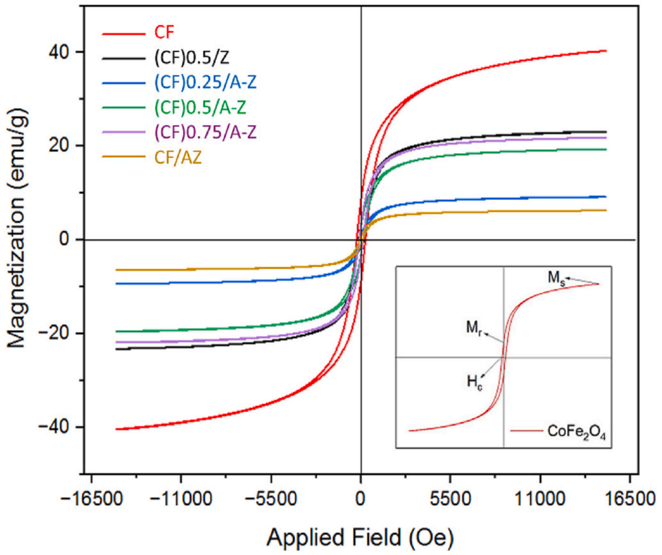

Fig. 8. Magnetic Hysteresis loops for $CoFe_2O_4$ inset and compared with various $(CoFe_2O_4)_x/Ag_2S$-ZnO samples.

together with the disordered surface spins of the Ag_2S-ZnO [51]. An increase in magnetic saturation was observed as the ratio concentration of $CoFe_2O_4$ was increased from 0.25 to 0.75. This was ascribed to the presence of the ferrite compounds, which act as the centre of the magnetic field. However, for sample $CoFe_2O_4/Ag_2S$-ZnO, a drastic drop in saturation as well as remanent magnetization was observed. The hysteresis loop analysis of the $CoFe_2O_4/Ag_2S$-ZnO composite demonstrates a relatively low saturation magnetization (Ms) value of 6.51 emu/g, which is lower compared to the $(CoFe_2O_4)_{0.5}/Ag_2S$-ZnO nanocomposite (19.44 emu/g). This finding suggests that the magnetic properties of the $(CoFe_2O_4)_{0.5}/Ag_2S$-ZnO nanocomposite primarily arise from the presence of magnetic CoFe2O4 incorporated within the Ag_2S-ZnO structure. A related study by Hassani et al. [52] reported a significant increase in magnetic saturation from 0.44 emu/g to 5.24 emu/g when $CoFe_2O_4$ nanoparticles were introduced into a reduced-GO nanocomposite.

The extracted parameters presented in Table 2 show that, pristine $CoFe_2O_4$ exhibited a higher coercivity than the other samples. According to previous studies, the difference in H_C values can be attributed to several intrinsic and extrinsic factors like particle size, microstructure, magneto-crystallinity, anisotropy constant and chemical composition [51,53].

Table 2 summarises the magnetic parameters obtained and calculated for each of the photocatalyst samples. The magnetic anisotropy constant K, which depends on the saturation magnetization and the coercivity of the samples was calculated following the expression [54] given by Eq.

$$K = \frac{H_C \times M_S}{0.96} \tag{5}$$

The S-shaped loops of the magnetic hysteresis curves, low values of remanent magnetization and coercivity as observed in all the samples, is a clear indication that ferrimagnetic materials were synthesised.

4. Photocatalytic degradation studies

4.1. *Visible-light photodegradation of MB dye*

Prior to the degradation investigations of MB, control experiments were conducted to establish the degradation potential of the light source used as well as the adsorption capacity of the various synthesised nanocomposites. Photolysis (pollutant and visible light only) recorded 6.2 % MB dye degradation while adsorption of each of the nanocomposites resulted in <16 % MB dye removal. Fig. 9 shows the results from the photolysis test together with a representation of the highest adsorption performance obtained by $(CoFe_2O_4)_{0.5}/Ag_2S$-ZnO.

The photocatalytic performance of each of the synthesised nanocomposite was tested under the same experimental conditions. The extent of degradation recorded after 240 min of visible irradiation for ZnO, $CoFe_2O_4$, $(CoFe_2O_4)_{0.5}$/ZnO, Ag_2S-ZnO, $(CoFe_2O_4)_{0.25}/Ag_2S$-ZnO, $(CoFe_2O_4)_{0.5}/Ag_2S$-ZnO, $(CoFe_2O_4)_{0.75}/Ag_2S$-ZnO and $CoFe_2O_4/Ag_2S$-ZnO were 55.93 %, 23.67 %, 44.9 %, 99.2 %, 97.3 %, 98.91 %, 90.07 % and 85.52 % respectively. The high performance of AZ than the other composites was due to the effect of a lower bandgap energy [32]. Theoretically, it was expected that the low direct optical bandgap of $CoFe_2O_4$ (~1.58 to 2.56 eV) would further narrow the overall bandgap of $(CoFe_2O_4)_x/Ag_2S$-ZnO blend and increase the photosensitivity towards the visible-light region [55]. However, a gradual relapse in photocatalytic activity was observed relative to an increase in the $(CoFe_2O_4)_x/Ag_2S$-ZnO combination ratio. This can be attributed to a reduction of bandgap energy levels and decreasing alteration in the particle crystallite sizes of the synthesised composites as confirmed by

Table 2
Magnetic parameters of the synthesised nanocomposites.

Samples	M_S (emu/g)	M_r (emu/g)	H_C (Oe)	SQ (M_r/M_S)	K (erg/Oe)
$CoFe_2O_4$	40.52	8.62	268.41	0.213	11,329.14
$(CoFe_2O_4)_{0.5}$/ZnO	22.98	3.42	136.58	0.149	3269.38
$(CoFe_2O_4)_{0.25}/Ag_2S$-ZnO	9.23	0.98	93.03	0.106	1244.45
$(CoFe_2O_4)_{0.5}/Ag_2S$-ZnO	19.44	2.95	125.93	0.152	2550.08
$(CoFe_2O_4)_{0.75}/Ag_2S$-ZnO	21.96	3.43	120.49	0.156	2756.21
$CoFe_2O_4/Ag_2S$-ZnO	6.51	0.79	94.24	0.121	639.07

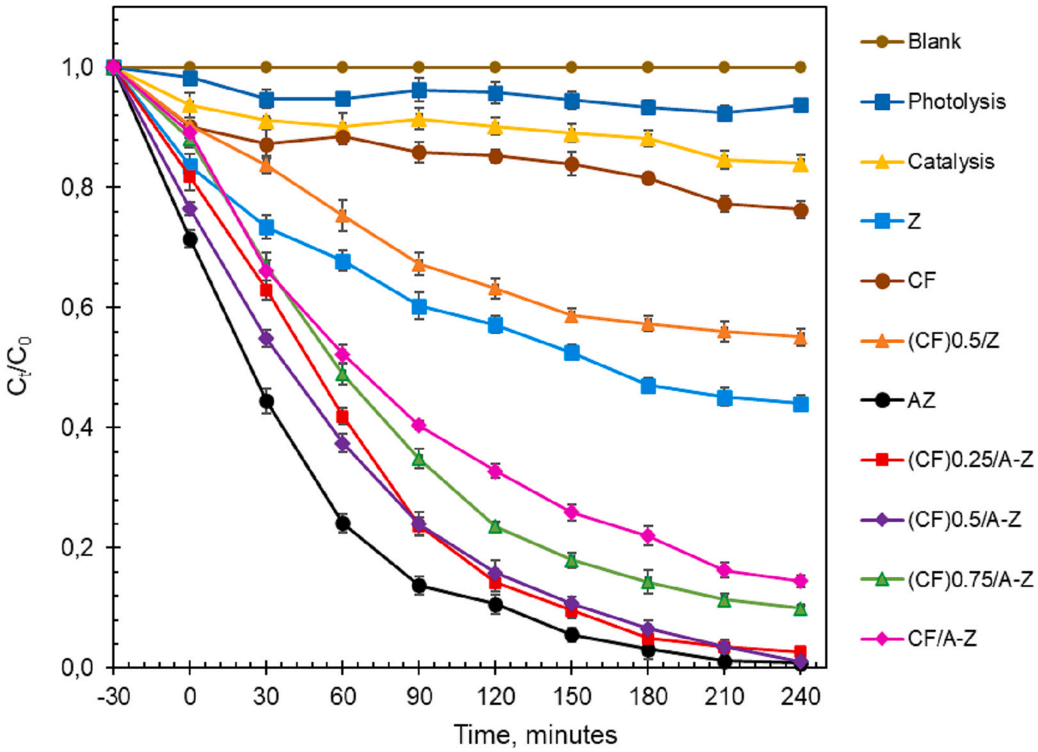

Fig. 9. Photolysis, catalysis of Ag_2S-ZnO and photocatalytic degradation of MB dye using various as-synthesised individual $(CoFe_2O_4)_x/Ag_2S$-ZnO nanocomposites.

the UV–vis DRS and XRD results. The estimates of bandgap energy obtained from the UV–vis Tauc plots suggests a gradual shift of photocatalytic activity of the composites from visible-light to UV region. Additionally, the SEM image for $CoFe_2O_4/Ag_2S$-ZnO suggests that, its agglomerated morphology could be responsible for the reduced photocatalytic activity as a higher porosity provides more active sites for an improved reactional activity [56].

Catalyst dosage and pH level of the reaction medium are the major intrinsic parameters that affects photocatalytic degradation efficiency of dyes [57]. Optimization tests were conducted by varying the amount of the best performing ternary $(CoFe_2O_4)_{0.5}/Ag_2S$-ZnO composite from 0.25 to 1.25 gL^{-1} at a 10 ppm of MB dye in water. From Fig. 10a, the results showed optimum degradation efficiency of 99 % and 98.9 % MB dye removal at 1 gL^{-1} and 1.25 gL^{-1} respectively. However, the consecutive decline in performance for the lower catalyst doses is attributed to the absence of sufficient surface active sites, decreased generation of free radicals, and high light-scattering effects [58]. Whereas a further increase of catalyst loading did not improve the photodegradation efficiency but increased the turbidity level and limited the effect of light penetration/scattering [59]. In a related study investigating the degradation of Azurobine using Fe_2O_3@multi-walled carbon nanotube activated peroxymonosulfate, it was found that the degradation rate declined as the catalyst dosage increased from 0.05 gL^{-1} to 0.17 gL^{-1} [60]. The optimal performance was observed at a catalyst dosage of 0.13 gL^{-1}, indicating that further increases in dosage resulted in agglomeration of the catalyst particles, leading to a reduction in active sites and consequently decreasing the degradation efficiency. Based on these findings, the optimal catalyst dosage for the current study was determined to be 1 gL^{-1}.

The pH level of MB dye solution was adjusted by dropwise addition of 0.2 M HCl (acidic) or Na•• (basic) to a range of 3 to 11 pH conditions, and tested using 1 gL^{-1} of $(CoFe_2O_4)_{0.5}/Ag_2S$-ZnO catalyst. The results presented in Fig. 10b showed that at highly acidic condition of pH 3, only 18.75 % of MB dye degraded. This was likely due to electrostatic positive charge repulsion between molecules of MB dye, which are predominately cationic under acidic conditions and the protonated catalyst surface [61]. At extreme alkaline conditions of pH 11, the removal of MB dye was 81.34 %. The highest MB dye degradation efficiency of 98.69 % was achieved at neutral pH. Furthermore, it is postulated that the synergistic interplay occurring on the catalyst's surface between the photogenerated reactive species and the target pollutant plays a crucial role in determining the efficacy of the photodegradation process [62]. Colloidal particles inherently possess an overall surface charge, which exerts a significant influence on the adsorption process. The overall surface charge of the catalyst is modulated by the pH of the surrounding medium [61]. The $(CoFe_2O_4)_{0.5}/Ag_2S$-ZnO nanoparticles possess excellent water dispersibility across a wide pH range. Zeta potential (ζ) values of the $(CoFe_2O_4)_{0.5}/Ag_2S$-ZnO nanoparticles were measured at different pH levels (ranging from 1 to 11) and depicted in Fig. 10e. The magnitude of ζ serves as an indicator of the surface charge carried by the nanoparticles, where higher or lower values correspond to increased or decreased electrostatic repulsion between the particles. In the case of magnetic nanoparticles, this electrostatic repulsion counteracts the magnetic attraction between them [62]. As the pH is gradually increased from 1, the absolute value of ζ diminishes and reaches its minimum around pH 3. At this point, the magnetic attraction dominates over the electrostatic repulsion, resulting in enhanced agglomeration of the $(CoFe_2O_4)_{0.5}/Ag_2S$-ZnO nanoparticles. However, beyond pH 3, the absolute value of ζ starts to rise, intensifying the electrostatic repulsion among the nanoparticles and leading to a decrease in the available active surface area for reactions. Around pH 9, the ζ value becomes significantly negative (−23.4 mV), indicating an abundance of negative charges on the surface of the $(CoFe_2O_4)_{0.5}/Ag_2S$-ZnO nanoparticles. The pH at the point of zero charge (pH_{PZC}) for $(CoFe_2O_4)_{0.5}/Ag_2S$-ZnO was experimentally determined as 3.24.

The results obtained from the optimization of catalyst dosage and pH conditions were found to follow a pseudo-first-order kinetic model, which correlates, to the Langmuir-Hinshelwood (L-H) degradation kinetic model for heterogeneous photocatalytic surface reactions expressed by Eq. (6):

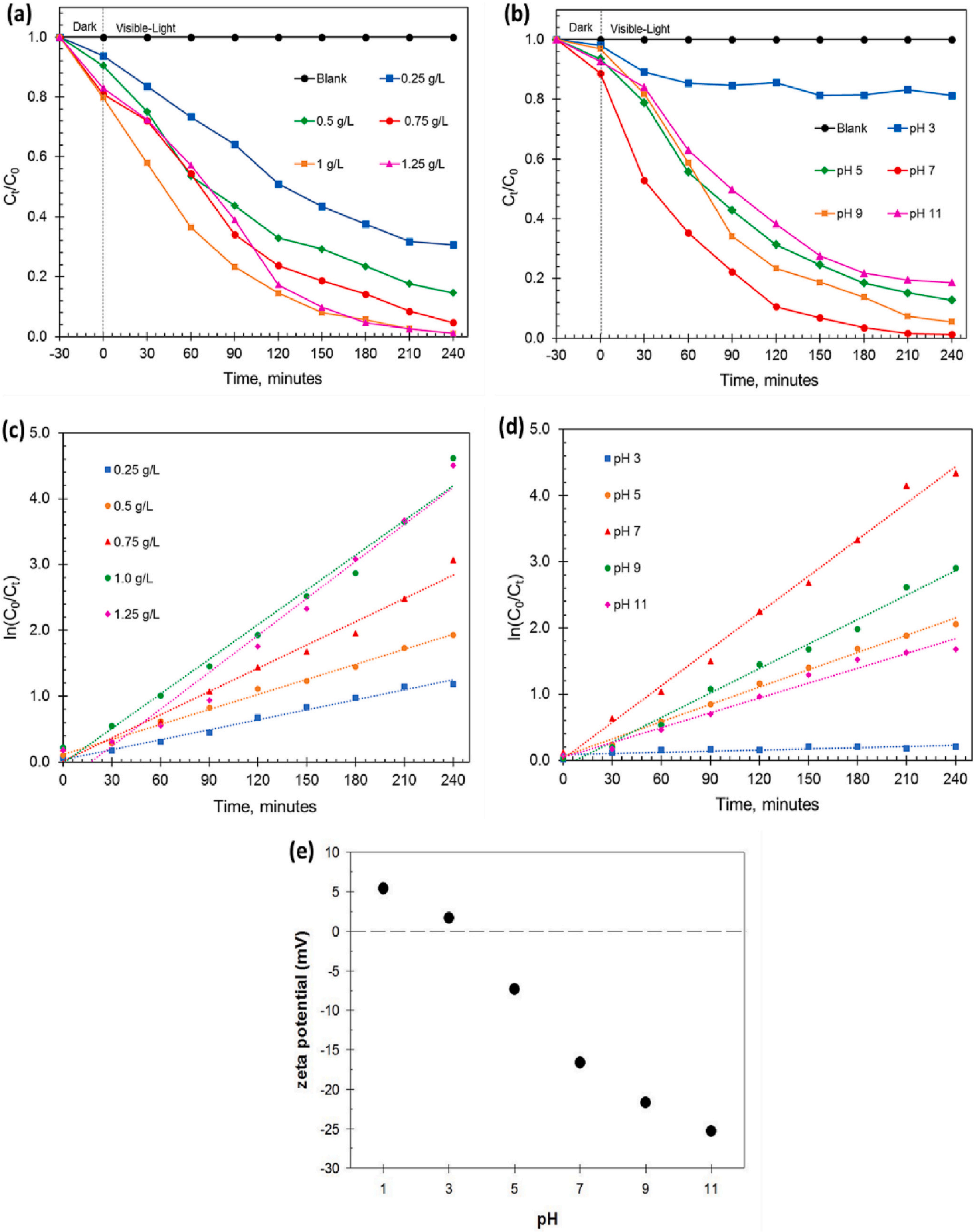

Fig. 10. Optimization tests and kinetic curves of varying (a, c) catalyst dosage and (b, d) pH level in the removal of MB dye using $(CoFe_2O_4)_{0.5}/Ag_2S\text{-}ZnO$ nanocomposite; (e) Effect of pH on the zeta potential of $(CoFe_2O_4)_{0.5}/Ag_2S\text{-}ZnO$ nanocomposite.

$$r = -\frac{dC}{dt} = k_{max}C_{MB\ dye} \rightarrow ln\left(\frac{C_0}{C_t}\right) = kt + 1 \tag{6}$$

where k (min^{-1}) is the reaction rate constant, C_0 and C_t are the initial and final MB dye concentration and t is the reaction time (min). To further confirm the best fitting data and test the uniform distribution of a "no hypothesis" or "alternative hypothesis" fit of the kinetic model, Chi-square test, (x_c^2), was applied following the expression represented by Eq. (7):

$$x_c^2 = \frac{\sum (Observed - Expected)^2}{Expected} \tag{7}$$

This was determined using the experimentally obtained results and an expected complete MB dye decolourisation at a 5 % significance level. The degree of freedom, (df = n − 1) was estimated based on the number of categories (n) and the area to the right of the critical value, (C_V), was obtained from the chi-square distribution table.

Fig. 10c and d show the linear fits of the L-H kinetic model of different catalyst dosages and various pH conditions respectively. All the catalyst dosage variations were found to follow a linear profile with exceptionally high values of the correlation coefficient ($R^2 \geq 0.96$) as shown in Table 3. All the chi-square values lie in the "do not reject" area, which accepts a "no hypothesis" that the results were obtained with relatively equal frequencies.

In contrast, the optimization of pH level tests as listed in Table 4 showed a nonlinear profile with extremely low value of correlation coefficient at pH 3 suggesting that the kinetic model does not fit for all pH levels. However, at higher pH levels (5, 7, 9 and 11), the R^2 values were >0.9, which indicates a favourable photodegradation activity of MB dye at alkaline conditions. The chi-square value for pH 3 lies deeply to the right of the C_V in the "rejection region" and therefore rejects the "no hypothesis". Hence, the effectiveness of the photocatalyst for MB dye removal is significant to the variation of pH level and accepts an "alternative hypothesis". To summarise, 1 gL^{-1} of $(CoFe_2O_4)_{0.5}/Ag_2S$-ZnO catalyst presented an excellent MB dye removal efficiency of 99 % at a neutral pH level under 4 h of visible light irradiation.

4.2. Reusability of the magnetic $(CoFe_2O_4)_{0.5}/Ag_2S$-ZnO nanocatalyst

The $(CoFe_2O_4)_{0.5}/Ag_2S$-ZnO composite showed excellent stability in the removal of MB dye with 95.3 % degradation occurring after five recycle run (Fig. 11a). A 3.7 % decrease in photocatalytic performance was observed between the first and fifth run. Previous studies have attributed the loss of activity during recycle runs to the blocking of surface active sites by MB dye intermediates [63]. As a result, the blockage hinders the rapid diffusion of fresh dye molecules through the inner pores to the surface of the photocatalyst. Fig. 11b–d, compare the SEM images and XRD patterns of the fresh $(CoFe_2O_4)_{0.5}/Ag_2S$-ZnO photocatalyst and the one recovered after 5 degradation cycles. No significant differences were noted in both analyses. This indicates that not only was the catalyst easily recoverable due to the magnetic properties imparted by the CF, the material was also highly stable and could be used to degrade organic pollutants efficiently multiple times.

Table 3

Parameters for kinetic modelling based on catalyst dosage of $(CoFe_2O_4)_{0.5}/Ag_2S$-ZnO.

Catalyst dosage (gL^{-1})	Reaction rate constant, k (min^{-1})	Correlation coefficient, R^2	Chi-square test, x_c^2 $C_V = 9.490$	MB dye removal %
0.25	0.00856	0.9658	6.899	69.4
0.5	0.01124	0.9791	0.970	85.4
0.75	0.01479	0.9806	0.0009	95.3
1	0.01966	0.9948	0.168	99.0
1.25	0.01854	0.9899	0.160	98.9

Table 4

Parameters for the reaction kinetic modelling based on pH level for catalyst $(CoFe_2O_4)_{0.5}/Ag_2S$-ZnO.

pH level (1 (gL^{-1}))	Reaction rate constant, k (min^{-1})	Correlation coefficient, R^2	Chi-square test, x_c^2 $C_V = 9.490$	MB dye removal %
3	0.00483	0.6886	61.120	18.8
5	0.01987	0.9762	0.640	87.2
7	0.01518	0.9924	0.144	98.7
9	0.01263	0.9899	0.003	94.5
11	0.01119	0.9774	1.976	81.3

4.3. Dye degradation pathways and mechanism

Fig. 12a demonstrates the impact of different scavengers on the degradation performance of methylene blue (MB) dye during photocatalytic treatment. The addition of triethanolamine (TEA) significantly decreased the dye removal efficiency to 17.45 % compared to the 99 % achieved without any scavengers. This substantial reduction can be attributed to the rapid electron transfer to the photocatalyst's surface, which leads to a limited number of available holes (h_{VB}^+) responsible for generating hydroxyl radicals (•OH). The significant loss of activity indicates that h^+ plays a crucial role as the primary active species in efficient MB dye photocatalytic degradation. The introduction of C_2N had a minimal effect on the degradation efficiency, with 93.6 % MB dye removal achieved. However, the presence of pBZQ and IPA decreased the degradation efficiencies to 75.2 % and 78.8 % respectively, indicating that they contribute as secondary actors to the activity of the $•O_2^-$ and •OH radicals in the degradation process. This outcome highlights that in the $(CoFe_2O_4)_{0.5}/Ag_2S$-ZnO photocatalytic degradation system, the degradation of MB primarily occurs through the synergistic action of •OH, h^+, and $•O_2^-$ radicals.

The outcomes of the active species scavenging experiments conducted in this study are consistent with a previous investigation on the degradation of methylene blue (MB) utilizing Ag-Cu_2O [64]. In the cited study, the researchers utilized a Shimadzu GC–MS instrument (GCMS-QP2010SE) to detect and perform comprehensive analysis on seven intermediate products. The intermediates were identified (labelled A–G) based on their *m/z* ratios corresponding to the results reported for the photocatalytic degradation of MB. Fig. 12b illustrates the two primary degradation pathways proposed by the authors, one involving the direct attack of holes and the other involving the oxidation by hydroxyl radicals.

Photocatalytic degradation occurs when light photons interact with the photocatalyst suspended in an aqueous solution containing the target organic pollutant molecules. These photons contain energy (*hv*) which is adsorbed by the catalyst and excites electrons (e^-) from the low energy filled valence band (V_B) to a higher energy empty conduction band (C_B) leaving holes (h^+) behind in the V_B as shown in Fig. 13 [65]. These photo-generated e^-/h^+ pairs are responsible for the breakdown of molecules of the pollutant through a series of reduction-oxidation (redox) reactions that mainly occur on the surface of the photocatalyst. During redox reactions, the photo-generated electrons at the C_B absorbs dissolved oxygen (O_2) from moisture in the air and reduces them to superoxide $\left(O_2^{\cdot-}\right)$ radicals while the holes at the V_B react with water (H_2O) to produce hydroxyl free radicals (OH•). These free radicals, which are typically formed on the surface of the photocatalyst, oxidise and react with the MB dye pollutant molecules absorbed on the catalyst surface, this interaction results in the formation of intermediate compounds or complete mineralization to CO_2 and H_2O only [66]. It should be noted that the $O_2^{\cdot-}$ radical not only supports pollutant oxidation but it may also inhibit e^-/h^+ pair recombination by upholding a neutrality between the charges within the molecule of the photocatalyst [67]. This is achieved through the protonation of the $O_2^{\cdot-}$ to form hydroperoxyl radical (HOO•) which dissociates to form hydrogen peroxide (H_2O_2) and

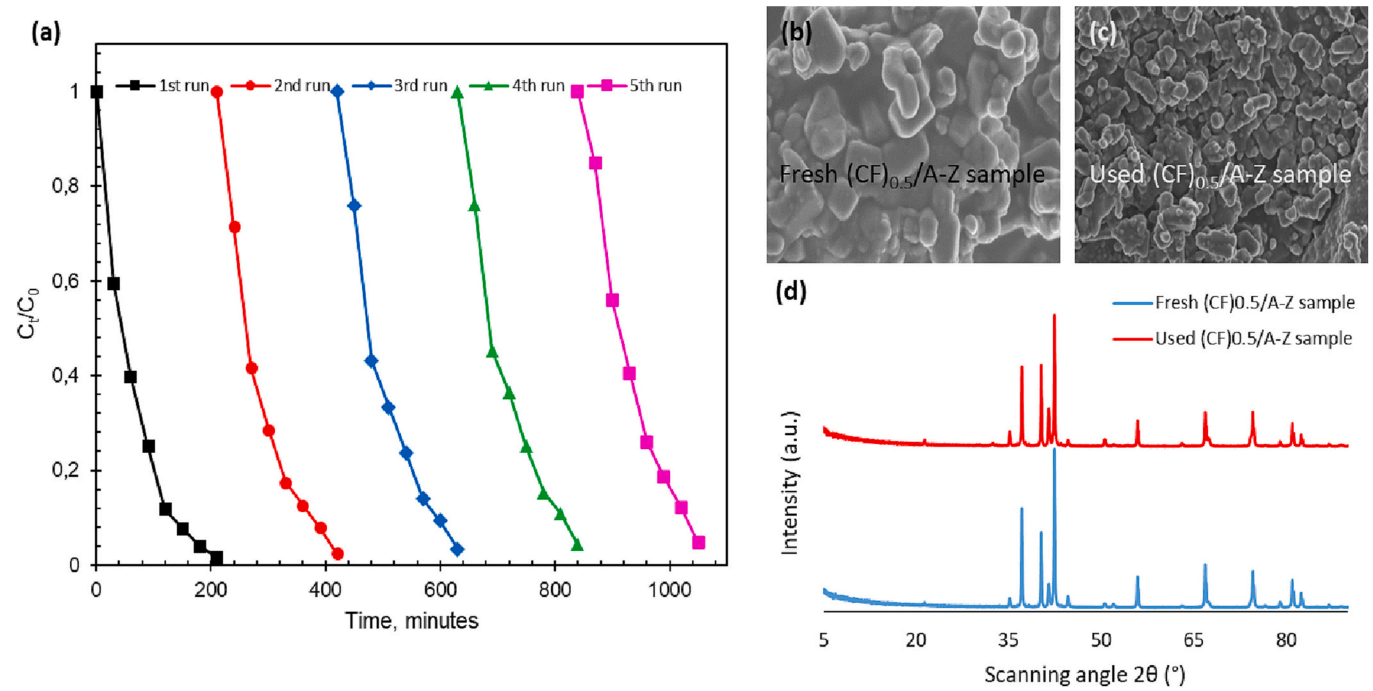

Fig. 11. (a) Recycling tests for MB dye removal; SEM images of $(CoFe_2O_4)_{0.5}/Ag_2S$-ZnO (b) fresh and (c) used after 5 cycles; compared XRD patterns of fresh and used $(CoFe_2O_4)_{0.5}/Ag_2S$-ZnO nanocomposites.

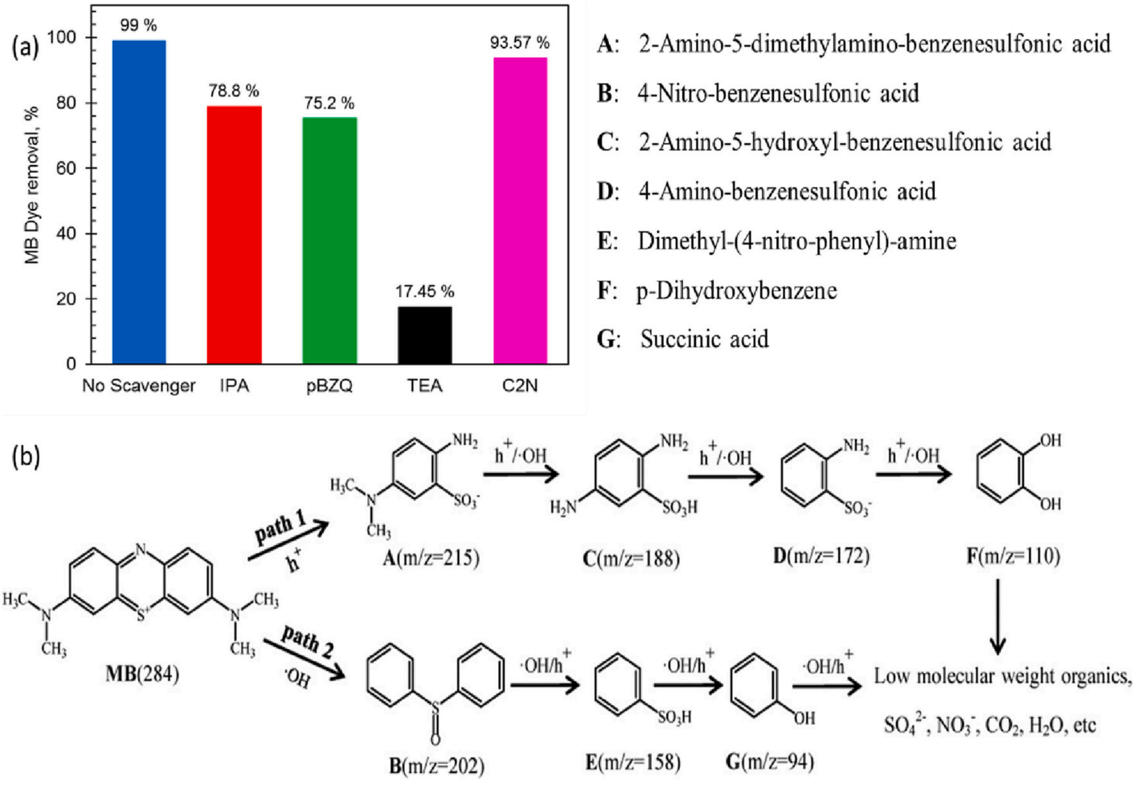

Fig. 12. (a) Effect of reactive photo-induced species scavengers; (b) Representation of possible MB degradation pathways [64].

finally highly reactive OH• radicals. The MB dye degradation mechanism using $(CoFe_2O_4)_{0.5}/Ag_2S$-ZnO photocatalyst can be summarised below with the availability of holes (h^+) being the rate-determining step as evidenced from the scavenger tests.

$$(CF)_{0.5}/AZ + h\nu \rightarrow (CF)_{0.5}/AZ\left(e^-_{CB} + h^+_{VB}\right) \quad (8)$$

$$H_2O + h^+_{VB} \rightarrow OH^{\cdot} + H^+ \quad (9)$$

$$O_2 + e^-_{CB} \rightarrow O_2^{\cdot -} \quad (10)$$

$$O_2^{\cdot -} + H^+ \leftrightarrow HOO^{\cdot} \quad (11)$$

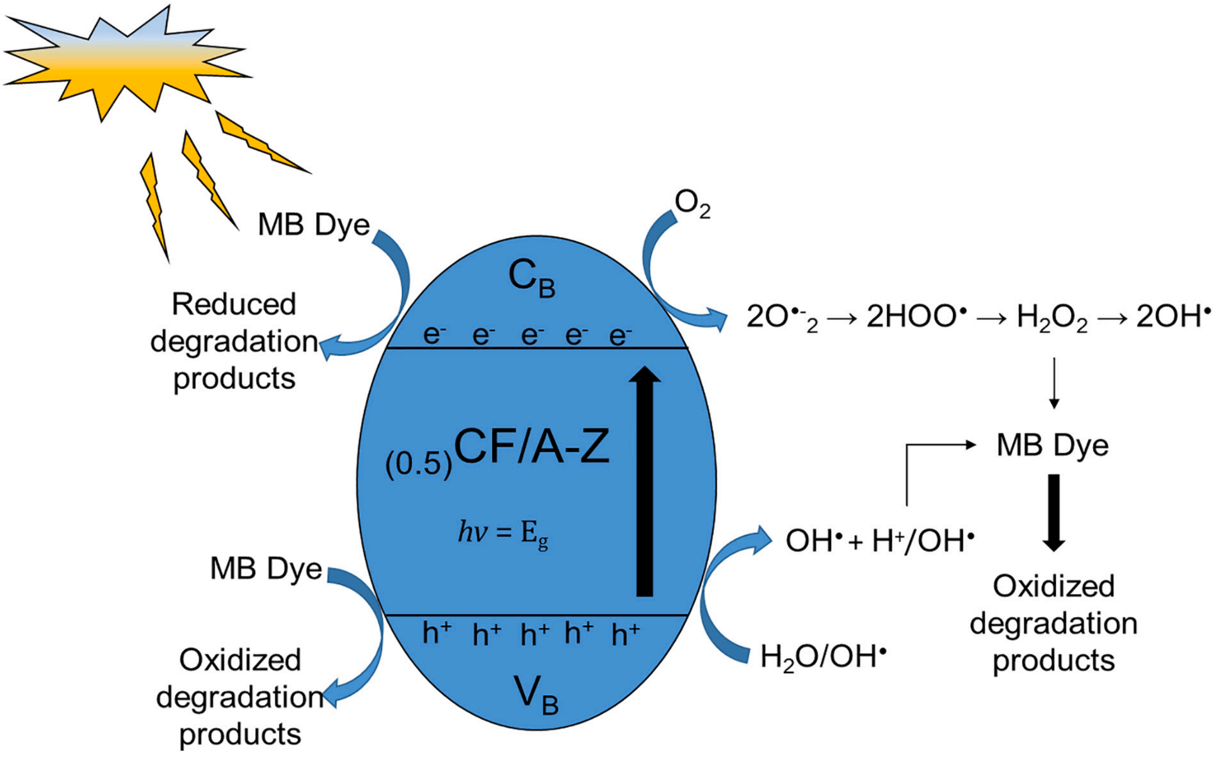

Fig. 13. Illustration of the degradation mechanism of $(CoFe_2O_4)_{0.5}/Ag_2S\text{-}ZnO$ photocatalyst.

$$2HOO^{\cdot} \rightarrow H_2O_2 + O_2 \tag{12}$$

$$\text{MB dye} + OH^{\cdot} \rightarrow CO_2 + H_2O \iddots \text{Intermediates} \tag{13}$$

$$\text{MB Dye} + h^{+}_{VB} + e^{-}_{CB} \rightarrow \text{Redox degradation products} \tag{14}$$

5. Conclusions

In this study, facile combustion and hydrothermal methods were followed to prepare $CoFe_2O_4$ and Ag_2S-ZnO nanoparticles. $(CoFe_2O_4)_x/Ag_2S$-ZnO nanocomposites were synthesised by mixing various ratios of both nanoparticle powders in a solvent, assisted by intense ultrasonication. The structural, optical, morphological, textural, and magnetic properties of the as-synthesised nanocomposites were studied. Optimization tests on core degradation parameters with intrinsic effect on the overall system performance achieved 99 % MB dye removal after 4 h under visible light irradiation. Under optimum conditions, $(CoFe_2O_4)_{0.5}/Ag_2S$-ZnO exhibited excellent chemical stability and recyclability after five runs without any significant alteration in its structural and morphological properties observed. Degradation scavenging investigations identified the holes, hydroxyl ions and superoxide free radicals as the main species responsible for the performance of $(CoFe_2O_4)_{0.5}/Ag_2S$-ZnO. Overall, this study confirms that the $(CoFe_2O_4)_{0.5}/Ag_2S$-ZnO composite catalyst is an efficient, easily recoverable material that can be used in sustainable water and wastewater treatment applications.

CRediT authorship contribution statement

Emmanuel O. Ichipi: Methodology, Formal analysis, Investigation, Visualisation, Data curation, Roles/writing - original draft, Writing – review and editing and Project administration. **António B. Mapossa:** Conceptualisation, Methodology, Data curation, Investigation, Supervision, Writing – review and editing, and Project administration. **Ana Cristina F.M. Costa:** Methodology, Investigation, Writing – review and editing. **Shepherd M. Tichapondwa:** Conceptualisation, Validation, Formal analysis, Supervision, Writing – review and editing, Data curation, Supervision, Funding and Project administration. **Evans M. N. Chirwa:** Funding acquisition, Resources, Supervision, Validation, Writing – review and editing.

Declaration of competing interest

The authors hereby declare that they have NO affiliations with or involvement in any organization or entity with any financial interest (such as honoraria; educational grants; participation in speakers' bureaus; membership, employment, consultancies, stock ownership, or other equity interest; and expert testimony or patent-licensing arrangements), or non-financial interest (such as personal or professional relationships, affiliations, knowledge or beliefs) in the subject matter or materials discussed in this manuscript.

Data availability

Data will be made available on request.

Acknowledgements

This work was supported by the National Research Foundation of South Africa (Grant numbers: CSUR180215313534, TTK18024324064) and Sedibeng Water Chair awarded to Prof Evans MN Chirwa and Prof Shepherd SM Tichapondwa.

References

[1] R. Kishor, D. Purchase, G.D. Saratale, R.G. Saratale, L.F.R. Ferreira, M. Bilal, R. Chandra, R.N. Bharagava, Ecotoxicological and health concerns of persistent coloring pollutants of textile industry wastewater and treatment approaches for environmental safety, J. Environ. Chem. Eng. 9 (2) (2021) 105012, https://doi.org/10.1016/j.jece.2020.105012.

[2] A. Kalra, A. Gupta, Recent advances in decolourization of dyes using iron nanoparticles: a mini review, Materials Today: Proc. 36 (2021) 689–696, https://doi.org/10.1016/j.matpr.2020.04.677.

[3] C. Tizaoui, N. Grima, Kinetics of the ozone oxidation of Reactive Orange 16 azo-dye in aqueous solution, Chem. Eng. J. 173 (2) (2011) 463–473, https://doi.org/10.1016/j.cej.2011.08.014.

[4] J. Hassan, Md.M.R. Rajib, U. Sarker, M. Akter, Md.N.E.A. Khan, S. Khandaker, F. Khalid, G.K.M. Rahman, S. Ercisli, C.C. Muresan, R.A. Marc, Optimizing textile dyeing wastewater for tomato irrigation through physiochemical, plant nutrient uses and pollution load index of irrigated soil, Sci. Rep. 12 (1) (2022) 1–18, https://doi.org/10.1038/s41598-022-11558-1.

[5] P.K. Jain, A.K. Sharma, N. Agarwal, P.K. Jain, N.S. Sengar, N. Agarwal, M. Z. Siddiqui, P. Pawal, A.K. Singh, R.D. Gaba, A prospective clinical study of myocarditis in cases of acute ingestion of paraphenylene diamine (hair dye) poisoning in northern India, J. Assoc. Physicians India 61 (9) (2013) 633–636.

[6] L.M. Fjellsbø, AnR.V., J. Rompay, I. Hooyberghs, M. Dusinska Nelissen, Screening for potential hazard effects from four nitramines on human eye and skin, Toxicol. in Vitro 27 (4) (2013) 1205–1210, https://doi.org/10.1016/j.tiv.2013.02.004.

[7] M. Peydayesh, M.K. Suter, S. Bolisetty, S. Boulos, S. Handschin, L. Nyström, R. Mezzenga, Amyloid fibrils aerogel for sustainable removal of organic contaminants from water, Adv. Mater. 32 (12) (2020) 1907932, https://doi.org/10.1002/adma.201907932.

[8] D. Bhatia, N.R. Sharma, J. Singh, R.S. Kanwar, Biological methods for textile dye removal from wastewater: a review, Crit. Rev. Environ. Sci. Technol. 47 (19) (2017) 1836–1876, https://doi.org/10.1080/10643389.2017.1393263.

[9] Q. Liu, Pollution and treatment of dye waste-water, in: IOP Conference Series: Earth and Environmental Science, IOP Publishing, 2020, https://doi.org/10.1088/1755-1315/514/5/052001.

[10] Y. Deng, R. Zhao, Advanced oxidation processes (AOPs) in wastewater treatment, Curr. Pollut. Rep. 1 (3) (2015) 167–176, https://doi.org/10.1007/s40726-015-0015-z.

[11] S. Li, C. Wang, Y. Liu, B. Xue, W. Jiang, Y. Liu, L. Mo, X. Chen, Photocatalytic degradation of antibiotics using a novel Ag/Ag$_2$S/Bi$_2$MoO$_6$ plasmonic p-n heterojunction photocatalyst: mineralization activity, degradation pathways and boosted charge separation mechanism, Chem. Eng. J. 415 (2021) 128991, https://doi.org/10.1016/j.cej.2021.128991.

[12] A.G. Akerdi, S.H. Bahrami, Application of heterogeneous nano-semiconductors for photocatalytic advanced oxidation of organic compounds: a review, J. Environ. Chem. Eng. 7 (5) (2019) 103283, https://doi.org/10.1016/j.jece.2019.103283.

[13] N. Pourshirband, A. Nezamzadeh-Ejhieh, An efficient Z-scheme CdS/g-C3N4 nano catalyst in methyl orange photodegradation: focus on the scavenging agent and mechanism, J. Mol. Liq. 335 (2021) 116543, https://doi.org/10.1016/j.molliq.2021.116543.

[14] M.A. Johar, R.A. Afzal, A.A. Alazba, U. Manzoor, Photocatalysis and bandgap engineering using ZnO nanocomposites, Adv. Mater. Sci. Eng. 2015 (2015) 1–22, https://doi.org/10.1155/2015/934587.

[15] R. Khokhra, B. Bharti, H.N. Lee, R. Kumar, Visible and UV photo-detection in ZnO nanostructured thin films via simple tuning of solution method, Sci. Rep. (2017), https://doi.org/10.1038/s41598-017-15125-x, 7.

[16] A. Hassani, S. Krishnan, J. Scaria, P. Eghbali, P.V. Nidheesh, Z-scheme photocatalysts for visible-light-driven pollutants degradation: a review on recent advancements, Curr. Opinion Solid State Mater. Sci. 25 (5) (2021) 100941, https://doi.org/10.1016/j.cossms.2021.100941.

[17] M. Kumar, S. Ambika, A. Hassani, P.V. Nidheesh, Waste to catalyst: role of agricultural waste in water and wastewater treatment, Sci. Total Environ. 858 (2023) 159762, https://doi.org/10.1016/j.scitotenv.2022.159762.

[18] A.B. Lavand, Y.S. Malghe, Synthesis, characterization, and visible light photocatalytic activity of nanosized carbon doped zinc oxide, Int. J. Photochem. 2015 (2015) 790153, https://doi.org/10.1155/2015/790153.

[19] A. Sirivallop, T. Areerob, S. Chiarakorn, Enhanced visible light photocatalytic activity of N and ag doped and co-doped TiO$_2$ synthesized by using an in-situ solvothermal method for gas phase ammonia removal, Catalysts 10 (2020) 251, https://doi.org/10.3390/catal10020251.

[20] N.K. Singh, S. Saha, A. Pal, Solar light-induced photocatalytic degradation of methyl red in an aqueous suspension of commercial ZnO: a green approach, Desalin. Water Treat. 53 (2) (2015) 501–514, https://doi.org/10.1080/19443994.2013.838520.

[21] A. Hassani, M. Faraji, P. Eghbali, Facile fabrication of mpg-C$_3$N$_4$/Ag/ZnO nanowires/Zn photocatalyst plates for photodegradation of dye pollutant, J. Photochem. Photobiol. A Chem. 400 (2020) 112665, https://doi.org/10.1016/j.jphotochem.2020.112665.

[22] P.Y. Motlagh, A. Khataee, A. Hassani, T.S. Rad, ZnFe-LDH/GO nanocomposite coated on the glass support as a highly efficient catalyst for visible light photodegradation of an emerging pollutant, J. Mol. Liq. 302 (2020) 112532, https://doi.org/10.1016/j.molliq.2020.112532.

[23] K. Sirirerkratana, P. Kemacheevakul, S. Chuangchote, Color removal from wastewater by photocatalytic process using titanium dioxide-coated glass, ceramic tile, and stainless steel sheets, J. Clean. Prod. 215 (2019) 123–130, https://doi.org/10.1016/j.molliq.2020.112532.

[24] A.B. Mapossa, W. Mhike, J.L. Adalima, S. Tichapondwa, Removal of organic dyes from water and wastewater using magnetic ferrite-based titanium oxide and zinc oxide nanocomposites: a review, Catalysts 11 (12) (2021) 1543, https://doi.org/10.3390/catal11121543.

[25] M. Shekofteh-Gohari, A. Habibi-Yangjeh, M. Abitorabi, A. Rouhi, Magnetically separable nanocomposites based on ZnO and their applications in photocatalytic processes: a review, Crit. Rev. Environ. Sci. Technol. 48 (10–12) (2018) 806–857, https://doi.org/10.1080/10643389.2018.1487227.

[26] Z. Zhu, H. Huang, L. Liu, F. Chen, N. Tian, Y. Zhang, H. Yu, Chemically bonded α-Fe$_2$O$_3$/Bi$_4$MO$_8$Cl dot-on-plate Z-scheme junction with strong internal electric field for selective photo-oxidation of aromatic alcohols, Angew. Chem. Int. Ed. 61 (26) (2022) e202203519, https://doi.org/10.1002/anie.202203519.

[27] Z. Wu, X. Chen, X. Liu, X. Yang, Y. Yang, A ternary magnetic recyclable ZnO/Fe$_3$O$_4$/g-C3N4 composite photocatalyst for efficient photodegradation of monoazo dye, Nanoscale Res. Lett. 14 (1) (2019) 147, https://doi.org/10.1186/s11671-019-2974-2.

[28] A. Panahi, R. Monsef, M.K. Imran, A.A. Mahdi, A.A.K. Ruhaima, M. Salavati-Niasari, TmVO4/Fe$_2$O$_3$ nanocomposites: sonochemical synthesis, characterization, and investigation of photocatalytic activity, Int. J. Hydrog. Energy 48 (10) (2023) 3916–3930, https://doi.org/10.1016/j.ijhydene.2022.10.226.

[29] M. Amiri, K. Eskandari, M. Salavati-Niasari, Magnetically retrievable ferrite nanoparticles in the catalysis application, Adv. Colloid Interf. Sci. 271 (2019) 101982, https://doi.org/10.1016/j.cis.2019.07.003.

[30] C.J. Li, J.N. Wang, B. Wang, J.R. Gong, Z. Lin, A novel magnetically separable TiO$_2$/CoFe$_2$O$_4$ nanofiber with high photocatalytic activity under UV–vis light, Mater. Res. Bull. 47 (2) (2012) 333–337, https://doi.org/10.1016/j.materresbull.2011.11.012.

[31] S.M. Moosavi, P. Molla-Abbasi, Z. Haji-Aghajani, Photo-catalyst CoFe$_2$O$_4$–TiO$_2$: application in photo-degradation of organic dyes and magnetic nanocomposite preparation, J. Mater. Sci. Mater. Electron. 27 (5) (2016) 4879–4886, https://doi.org/10.1007/s10854-016-4371-2.

[32] E.O. Ichipi, S.M. Tichapondwa, E.M. Chirwa, Plasmonic effect and bandgap tailoring of Ag/Ag$_2$S doped on ZnO nanocomposites for enhanced visible-light photocatalysis, Adv. Powder Technol. 33 (6) (2022) 103596, https://doi.org/10.1016/j.apt.2022.103596.

[33] E.O. Ichipi, S.M. Tichapondwa, E. Chirwa, Facile synthesis and characterisation of nanosized ZnO modified with Ag$_2$S for visible-light-induced phenol degradation, URI: http://hdl.handle.net/2263/81823, 2021.

[34] J. Dantas, E. Leal, A.B. Mapossa, A.S.A. Silva, A.C.F.dM. Costa, Synthesis, characterization and catalytic performance of mixed nanoferrites submitted to transesterification and esterification reaction using methyl and ethyl route for biodiesel production, Matéria (Rio de Janeiro) 21 (2016) 1080–1093, https://doi.org/10.1590/S1517-707620160004.0099.

[35] A.B. Mapossa, J. Dantas, M.R. Silva, R.H.G.A. Kiminami, A.C.F.dM. Costa, M. O. Daramola, Catalytic performance of NiFe$_2$O$_4$ and Ni$_{0.3}$Zn$_{0.7}$Fe$_2$O$_4$ magnetic nanoparticles during biodiesel production, Arab. J. Chem. 13 (2) (2020) 4462–4476, https://doi.org/10.1016/j.arabjc.2019.09.003.

[36] X. Wang, J. Liu, S. Leong, X. Lin, J. Wei, B. Kong, Y. Xu, Z.X. Low, J. Yao, H. Wang, Rapid construction of ZnO@ZIF-8 heterostructures with size-selective photocatalysis properties, ACS Appl. Mater. Interfaces (2016) 8, https://doi.org/10.1021/acsami.6b00028.

[37] E. Ferdosi, H. Bahiraei, D. Ghanbari, Investigation the photocatalytic activity of CoFe$_2$O$_4$/ZnO and CoFe$_2$O$_4$/ZnO/Ag nanocomposites for purification of dye pollutants, Sep. Purif. Technol. 211 (2019) 35–39, https://doi.org/10.1016/j.seppur.2018.09.054.

[38] T.J. Castro, S.W. da Silva, F. Nakagomi, N.S. Moura, A. Franco Jr., P.C. Morais, Structural and magnetic properties of ZnO–CoFe$_2$O$_4$ nanocomposites, J. Magn. Magn. Mater. 389 (2015) 27–33, https://doi.org/10.1016/j.jmmm.2015.04.036.

[39] G. Thiele, M. Poston, R. Brown, A case study in sizing nanoparticles, Micromeritics Instrument Corporation. . Available online: http://www.particletesting.com/library, 2010. (Accessed 1 January 2019).

[40] Z. Jiang, L. Feng, J. Zhu, Synthesis of magnetically recyclable porous CoFe$_2$O$_4$/Rh composites with large BET surface area for enhanced photocatalytic degradation of organic pollutant, Ceram. Int. 47 (13) (2021) 18140–18149, https://doi.org/10.1016/j.ceramint.2021.03.132.

[41] N. Li, M. Zheng, X. Chang, G. Ji, H. Lu, L. Xue, L. Pan, J. Cao, Preparation of magnetic CoFe$_2$O$_4$-functionalized graphene sheets via a facile hydrothermal method and their adsorption properties, J. Solid State Chem. 184 (4) (2011) 953–958, https://doi.org/10.1016/j.jssc.2011.01.014.

[42] A. Abbasi, H. Khojasteh, M. Hamadanian, M. Salavati-Niasari, Synthesis of CoFe$_2$O$_4$ nanoparticles and investigation of the temperature, surfactant, capping agent and time effects on the size and magnetic properties, J. Mater. Sci. Mater. Electron. (2016) 27, https://doi.org/10.1007/s10854-016-4383-y.

[43] M. Singh, M. Goyal, K. Devlal, Size and shape effects on the band gap of semiconductor compound nanomaterials, J. Taibah Univ. Sci. 12 (4) (2018) 470–475, https://doi.org/10.1080/16583655.2018.1473946.

[44] M. Benelmekki, Introduction to nanoparticles and nanotechnology, in: Designing Hybrid Nanoparticles, second edition, IOP Publishing, 2021.

[45] P. Paramasivan, P. Venkatesh, A novel approach: hydrothermal method of fine stabilized superparamagnetics of cobalt ferrite (CoFe$_2$O$_4$) nanoparticles, J. Supercond. Nov. Magn. (2016) 29, https://doi.org/10.1007/s10948-016-3586-z.

[46] J. Revathi, M. John Abel, V. Archana, T. Sumithra, R. Thiruneelakandan, J. Joseph Prince, Synthesis and characterization of CoFe$_2$O$_4$ and Ni-doped CoFe$_2$O$_4$ nanoparticles by chemical co-precipitation technique for photo-degradation of organic dyestuffs under direct sunlight, Phys. B Condens. Matter 587 (2020) 412136, https://doi.org/10.1016/j.physb.2020.412136.

[47] V. Bartůněk, D. Sedmidubský, Š. Huber, M. Švecová, P. Ulbrich, O. Jankovský, Synthesis and properties of nanosized stoichiometric cobalt ferrite spinel, Materials 11 (2018) 1241, https://doi.org/10.3390/ma11071241.

[48] A. Khan, Raman spectroscopic study of the ZnO nanostructures, J. Pak. Mater. Soc. 4 (1) (2010) 5–9.

[49] C. Chen, Y. Zheng, Y. Zhan, X. Lin, Q. Zheng, K. Wei, Enhanced Raman scattering and photocatalytic activity of Ag/ZnO heterojunction nanocrystals, Dalton Trans. 40 (37) (2011) 9566–9570, https://doi.org/10.1039/C1DT10799B.

[50] H. Abomostafa, A. Azab, M. Selim, Innovative synthesis of nickel nanoparticles in polystyrene matrix with enhanced optical and magnetic properties, J. Inorg. Organomet. Polym. Mater. 29 (6) (2019) 1983–1994, https://doi.org/10.1007/s10904-019-01157-5.

[51] T.A. Hameed, A.A. Azab, R.S. Ibrahim, K.E. Rady, Optimization, structural, optical and magnetic properties of $TiO_2/CoFe_2O_4$ nanocomposites, Ceram. Int. 48 (14) (2022) 20418–20425, https://doi.org/10.1016/j.ceramint.2022.03.327.

[52] A. Hassani, P. Eghbali, F. Mahdipour, S. Wacławek, K.Y.A. Lin, F. Ghanbari, Insights into the synergistic role of photocatalytic activation of peroxymonosulfate by UVA-LED irradiation over $CoFe_2O_4$-rGO nanocomposite towards effective Bisphenol A degradation: performance, mineralization, and activation mechanism, Chem. Eng. J. 453 (2023) 139556, https://doi.org/10.1016/j.cej.2022.139556.

[53] J. Sort, S. Suriñach, J.S. Muñoz, M.D. Baró, J. Nogués, G. Chouteau, V. Skumryev, G.C. Hadjipanayis, Improving the energy product of hard magnetic materials, Phys. Rev. B 65 (17) (2002) 174420, https://doi.org/10.1103/PhysRevB.65.174420.

[54] El Abouzir, M. Elansary, M. Belaiche, H. Jaziri, Magnetic and structural properties of single-phase Gd^{3+}-substituted Co–Mg ferrite nanoparticles, RSC Adv. 10 (19) (2020) 11244–11256, https://doi.org/10.1039/D0RA01841D.

[55] A.V. Ravindra, P. Padhan, W. Prellier, Electronic structure and optical band gap of $CoFe_2O_4$ thin films, Appl. Phys. Lett. (2012) 101, https://doi.org/10.1063/1.4759001.

[56] A.M. Cahino, R.G. Loureiro, J. Dantas, V.S. Madeira, P.C.R. Fernandes, Characterization and evaluation of ZnO/CuO catalyst in the degradation of methylene blue using solar radiation, Ceram. Int. 45 (11) (2019) 13628–13636, https://doi.org/10.1016/j.ceramint.2019.03.239.

[57] K.M. Reza, A.S.W. Kurny, F. Gulshan, Parameters affecting the photocatalytic degradation of dyes using TiO_2: a review, Appl Water Sci 7 (4) (2017) 1569–1578, https://doi.org/10.1007/s13201-015-0367-y.

[58] F. Aisien, A. Amenaghawon, E. Ekpenisi, Photocatalytic decolourisation of industrial wastewater from a soft drink company, J. Eng. Appl. Sci. 9 (2014) 11–16.

[59] A. Iqbal, N.H. Ibrahim, N.R.A. Rahman, K.A. Saharudin, F. Adam, S. Sreekantan, R. M. Yusop, N.F. Jaafar, L.D. Wilson, ZnO surface doping to enhance the photocatalytic activity of lithium titanate/TiO_2 for methylene blue photodegradation under visible light irradiation, Surfaces 3 (3) (2020) 301–318, https://doi.org/10.3390/surfaces3030022.

[60] S. Madihi-Bidgoli, S. Asadnezhad, A. Yaghoot-Nezhad, A. Hassani, Azurobine degradation using Fe_2O_3@multi-walled carbon nanotube activated peroxymonosulfate (PMS) under UVA-LED irradiation: performance, mechanism and environmental application, J. Environ. Chem. Eng. 9 (6) (2021) 106660, https://doi.org/10.1016/j.jece.2021.106660.

[61] A.F. Alkaim, A.M. Aljeboree, N.A. Alrazaq, S.J. Baqir, F.H. Hussein, A.J. Lilo, Effect of pH on adsorption and photocatalytic degradation efficiency of different catalysts on removal of methylene blue, Asian J. Chem. 26 (2014) 8445–8448, https://doi.org/10.14233/ajchem.2014.17908.

[62] S. Munjal, N. Khare, C. Nehate, V. Koul, Water dispersible $CoFe_2O_4$ nanoparticles with improved colloidal stability for biomedical applications, J. Magn. Magn. Mater. 404 (2016) 166–169, https://doi.org/10.1016/j.jmmm.2015.12.017.

[63] Y. Ao, J. Xu, D. Fu, X. Shen, C. Yuan, Low temperature preparation of anatase TiO_2-coated activated carbon, Colloids Surf. A Physicochem. Eng. Asp. 312 (2) (2008) 125–130, https://doi.org/10.1016/j.colsurfa.2007.06.039.

[64] X. Yu, J. Zhang, Y. Chen, Q. Ji, Y. Wei, J. Niu, Z. Yu, B. Yao, Ag-Cu_2O composite films with enhanced photocatalytic activities for methylene blue degradation: analysis of the mechanism and the degradation pathways, J. Environ. Chem. Eng. 9 (5) (2021) 106161, https://doi.org/10.1016/j.jece.2021.106161.

[65] R. Ameta, M.S. Solanki, S. Benjamin, S.C. Ameta, Photocatalysis, in: Advanced Oxidation Processes for Waste Water Treatment, Elsevier, 2018, pp. 135–175, https://doi.org/10.1016/B978-0-12-810499-6.00006-1.

[66] S. Velusamy, A. Roy, S. Sundaram, T.K. Mallick, A review on heavy metal ions and containing dyes removal through graphene oxide-based adsorption strategies for textile wastewater treatment, Chem. Rec. 21 (7) (2021) 1570–1610, https://doi.org/10.1002/tcr.202000153.

[67] A. Ajmal, I. Majeed, R.N. Malik, H. Idriss, M.A. Nadeem, Principles and mechanisms of photocatalytic dye degradation on TiO_2 based photocatalysts: a comparative overview, RSC Adv. 4 (70) (2014) 37003–37026, https://doi.org/10.1039/C4RA06658H.